RESEARCH ARTICLE

Key Points:
- Aquatic metabolism and longitudinal DIC input via upstream runoff were major sources sustaining the widespread river CO_2 supersaturation
- River CH_4 production and evasion hot spots were closely associated with urban point sources and highly discharge-dependent
- River CO_2 evasion offsets C uptake in the regional terrestrial ecosystem (up to 40%) and the river-dominated East China Sea (10%)

Carbon dioxide and methane dynamics in a human-dominated lowland coastal river network (Shanghai, China)

Zhongjie Yu[1,2,3] (iD), Dongqi Wang[1,2] (iD), Yangjie Li[1,2,4], Huanguang Deng[1,2,5], Beibei Hu[6], Mingwu Ye[1,2], Xuhui Zhou[7,8] (iD), Liangjun Da[7,9], Zhenlou Chen[1,2], and Shiyuan Xu[1,2]

[1]Key Laboratory of Geographic Information Science (Ministry of Education), East China Normal University, Shanghai, China, [2]School of Geographical Sciences, East China Normal University, Shanghai, China, [3]Now at Department of Geology and Environmental Science, University of Pittsburgh, Pittsburgh, Pennsylvania, USA, [4]Now at Second Institute of Oceanography, State Oceanic Administration, Hangzhou, China, [5]Now at School of Environment and Planning, Liaocheng University, Liaocheng, China, [6]College of Urban and Environment Science, Tianjin Normal University, Tianjin, China, [7]School of Ecological and Environmental Sciences, East China Normal University, Shanghai, China, [8]Center for Global Change and Ecological Forecasting, East China Normal University, Shanghai, China, [9]Shanghai Key Lab for Urban Ecological Processes and Eco-Restoration, East China Normal University, Shanghai, China

Abstract Evasion of carbon dioxide (CO_2) and methane (CH_4) in streams and rivers play a critical role in global carbon (C) cycle, offsetting the C uptake by terrestrial ecosystems. However, little is known about CO_2 and CH_4 dynamics in lowland coastal rivers profoundly modified by anthropogenic perturbations. Here we report results from a long-term, large-scale study of CO_2 and CH_4 partial pressures (pCO_2 and pCH_4) and evasion rates in the Shanghai river network. The spatiotemporal variabilities of pCO_2 and pCH_4 were examined along a land use gradient, and the annual CO_2 and CH_4 evasion were estimated to assess its role in regional C budget. During the study period (August 2009 to October 2011), the overall mean pCO_2 and median pCH_4 from 87 surveyed rivers were 5846 ± 2773 μatm and 241 μatm, respectively. Internal metabolic CO_2 production and dissolved inorganic carbon input via upstream runoff were the major sources sustaining the widespread CO_2 supersaturation, coupling pCO_2 to biogeochemical and hydrological controls, respectively. While CH_4 was oversaturated throughout the river network, CH_4 hot spots were concentrated in the small urban rivers and highly discharge-dependent. The Shanghai river network played a disproportionately important role in regional C budget, offsetting up to 40% of the regional terrestrial net ecosystem production and 10% of net C uptake in the river-dominated East China Sea fueled by anthropogenic nutrient input. Given the rapid urbanization in global coastal areas, more research is needed to quantify the role of lowland coastal rivers as a major landscape C source in global C budget.

1. Introduction

Streams and rivers are important conduits and reactors connecting the terrestrial biosphere and the oceans in the global carbon (C) cycle [*Cole et al.*, 2007]. It has recently been discovered that streams and rivers are CO_2 supersaturated and emitting about 1.8 Pg C yr^{-1} of CO_2 to the atmosphere [*Raymond et al.*, 2013], a flux greater than the transport of dissolved inorganic and organic C (DIC and DOC) and particulate organic C (POC) to the oceans (0.9 Pg C yr^{-1}) [*Battin et al.*, 2009; *Aufdenkampe et al.*, 2011]. While there is a growing consensus that degassed CO_2 in streams and rivers is originally from C leakage through the terrestrial-aquatic interface [*Öquist et al.*, 2009; *Hotchkiss et al.*, 2015], offsetting the C uptake by terrestrial ecosystems [*Butman et al.*, 2016], the spatiotemporal patterns of CO_2 saturation and evasion in streams and rivers exhibit great variability and are difficult to elucidate [*Raymond et al.*, 2013]. To date, lateral groundwater inputs of high CO_2 derived from soils and fringing wetlands [*Johnson et al.*, 2008; *Crawford et al.*, 2013; *Abril et al.*, 2014] and in-stream oxidation of allochthonous organic C (OC) [*Richey et al.*, 2002; *Mayorga et al.*, 2005] are considered the two major sources sustaining the widespread CO_2 oversaturation and evasion in streams and rivers [*Hotchkiss et al.*, 2015] (see Figure S1 in the supporting information for a schematic). Additionally, longitudinal transport of DIC originating from terrestrial ecosystems via upstream runoff can also be an external contributor to CO_2 evasion in

downstream river segments [*Abril et al.*, 2014; *Gómez-Gener et al.*, 2016] (Figure S1). This longitudinal flux may be particularly important in high-alkalinity watersheds because of the carbonate buffering effect that diminishes CO_2 evasion rates, resulting in more consistent CO_2 concentration moving from small upstream waters to downstream rivers [*Stets et al.*, 2017] (Figure S1). Therefore, the relative importance of these major CO_2 pathways is controlled by the interactions among climatological, hydrogeological, and biogeochemical processes [*Butman and Raymond*, 2011; *Striegl et al.*, 2012], as well as physical gas transfer at the air-water interface [*Alin et al.*, 2011; *Beaulieu et al.*, 2012; *Raymond et al.*, 2012], which all can vary substantially along a stream-river continuum [*Dubois et al.*, 2010; *Hotchkiss et al.*, 2015]. Table S1 in the supporting information is a compilation of recent findings on CO_2 dynamics in streams and rivers, highlighting that river CO_2 partial pressure (pCO_2) and evasion rate can vary over 3 orders of magnitude along the climate (i.e., boreal to temperate to tropical) and geomorphological (i.e., upland headwater stream to lowland river) gradients.

On the other hand, dynamics of methane (CH_4), the end product of obligatory anaerobic metabolisms, in streams and rivers has received much less attention than in lakes, reservoirs, and wetlands [*Tranvik et al.*, 2009; *Rasilo et al.*, 2015] partially due to the perception that flowing waters do not favor anaerobic CH_4 formation [*Campeau et al.*, 2014]. Nevertheless, there is growing evidence for significant CH_4 evasion from streams and rivers having high hydrologic connectivity with riparian soils [*Dinsmore et al.*, 2010] or long water residence time that allows burial and consequent anaerobic decomposition of OC [*Maeck et al.*, 2013; *Crawford et al.*, 2016] (Figure S1). Although CH_4 evasion from streams and rivers may be small in terms of C (Table S1), CH_4 is a more potent greenhouse gas than CO_2 over century time scales [*Intergovernmental Panel on Climate Change (IPCC)*, 2007]. Therefore, it is crucial to evaluate whether CH_4 evasion from streams and rivers can be potentially as important as CH_4 evasion from impounded waters in terms of offsetting the terrestrial C sink [*Bastviken et al.*, 2011; *Stanley et al.*, 2016].

With about 60% of the world population living along global coastal boundaries, coastal watersheds are increasingly threatened by a variety of anthropogenic perturbations that cause pollution and physical alterations of the aquatic environment [*Bianchi and Allison*, 2009]. There is a current knowledge gap as to whether and how river CO_2 and CH_4 dynamics are affected by land use change in lowland coastal watersheds [*Butman and Raymond*, 2011; *Pérez et al.*, 2015]. Perhaps, the most widespread disturbance in human-impacted rivers is the enrichment of nutrients and organic matter originating from enhanced soil erosion, fertilizer applications, and industrial and domestic sewage [*Hosen et al.*, 2014; *Butman et al.*, 2015], leading to aquatic net heterotrophy (i.e., gross primary production (GPP) < ecosystem respiration (ER)) [*Kaushal et al.*, 2014; *Smith and Kaushal*, 2015]. By compiling large data sets of river CH_4 concentration and evasion, *Stanley et al.* [2016] revealed positive correlations among CH_4, DOC, and ammonium (NH_4^+) concentrations in rivers draining urban landscapes, highlighting that OC- and NH_4^+-rich sewage discharges may fuel CH_4 production in urban rivers. On the other hand, it is unclear how aquatic metabolism as an internal source of CO_2 and CH_4 is coupled to the complex hydrological regime in lowland coastal rivers, which is coregulated by tidal motion, upstream runoff, and human alterations [*Zhai et al.*, 2007]. Whether the established dependence of CO_2 source contribution [*Hotchkiss et al.*, 2015] and evasion [*Butman and Raymond*, 2011] on stream (river) order is applicable to highly impacted lowland coastal rivers remains unresolved. Therefore, a mechanistic understanding of CO_2 and CH_4 dynamics in human-dominated lowland coastal river networks is vital for setting the stage for future modeling of the coupled terrestrial-aquatic C cycling that includes responses to anthropogenic perturbations [*Regnier et al.*, 2013].

In this study, we conducted a long-term, large-scale survey of CO_2 and CH_4 partial pressures and evasion rates in the Shanghai river network. This area is one of the world's largest lowland coastal watersheds subject to profound human perturbations [*Bianchi and Allison*, 2009] but was poorly accounted for in previous global river CO_2 tabulation due to a paucity of direct measurements [*Raymond et al.*, 2013]. In a companion paper, we have reported the riverine nitrogen enrichment and nitrous oxide (N_2O) dynamics [*Yu et al.*, 2013]. Here we explored the CO_2 and CH_4 dynamics in the Shanghai river network based on a land use gradient (headwater-suburban-urban-rural, see below), leading to insights into the sources of and processes controlling CO_2 and CH_4 evasions in the Shanghai river network and their role in regional C budget.
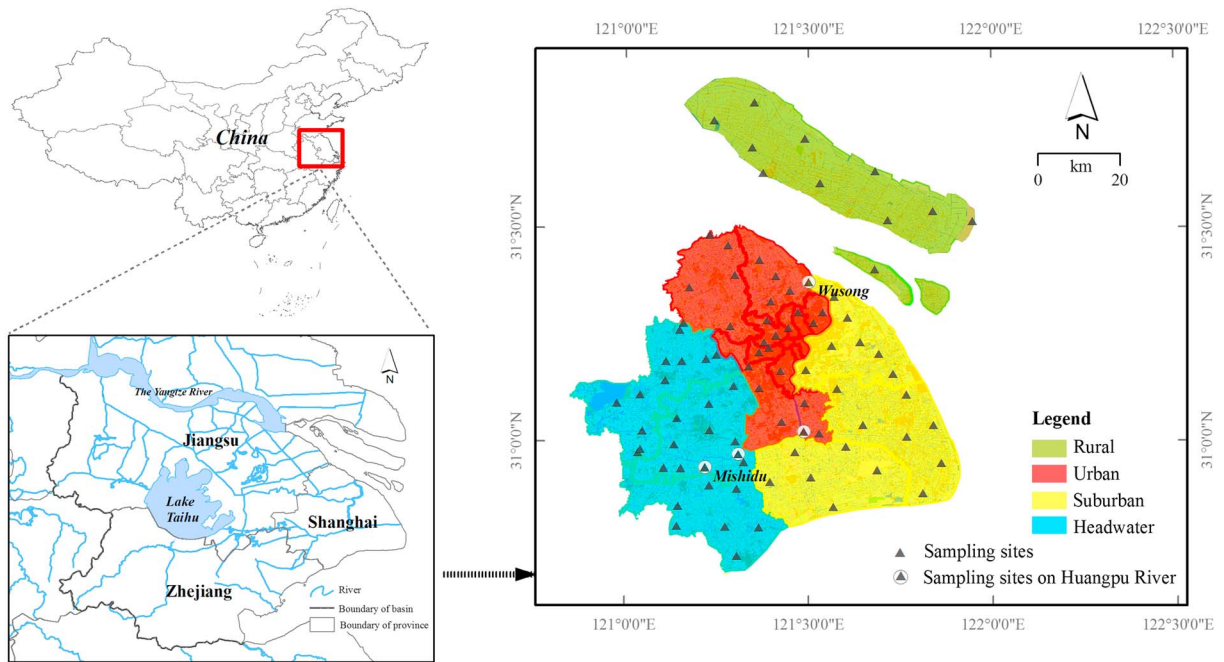
Figure 1. Location maps of the Taihu Lake basin and the Shanghai river network, highlighting the sampling sites in the four areas and the longitudinal transect of the Huangpu River.

2. Materials and Methods

2.1. Study Area

Shanghai is situated on the east tip of the Yangtze coastal plain (Figure 1). This region has a subtropical monsoon climate with higher temperature and about 70% of the annual precipitation occurring during the wet season (May to October) [*Chetelat et al.*, 2008; *Ran et al.*, 2017] (Figure 2). The mean annual temperature and precipitation are 15.5°C and 1466 mm, respectively (Figure 2). The elevation of this low-lying region ranges from 2.2 to 4.8 above mean sea level. The geology of this region is typical of tidal-dominated deltas with the Quaternary deposits consisting of five confined and one unconfined aquifers. The unconfined aquifer is about 8 m thick and has an annual mean water level of 0.5 to 1.5 m belowground surface [*Wu et al.*, 2014].
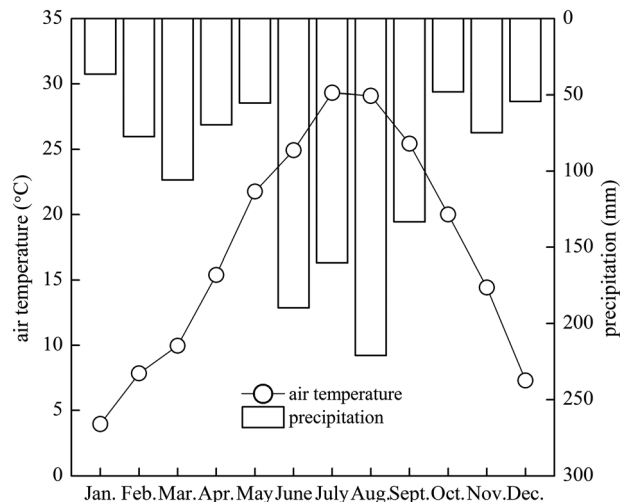

Figure 2. Monthly average of air temperature and precipitation during the study period.

Table 1. Hydromorphological Characteristics and Land Use Classification of the Shanghai River Network

District	Land Area (km^2)[a]	River Network Density (km km^{-2})[b]	Channel Storage (m^3 km^{-2})[b]	Riverbank Type[c]	Number of Sampling Site	Land Use (%)[a]			
						Urban	Industry	Agriculture	Green Land
Headwater Area									
Qingpu	669	3.2	9.3	N, C	11	14	8	53	5
Songjiang	606	3.2	9.3	N, C	11	19	12	54	5
Jinshan	586	4.5	4.7	N, C	7	17	6	66	2
Urban Area									
Downtown	207	0.9	0.9	C	10	68	16	1	5
Minghang	372	4.2	3.1	C	6	31	23	33	5
Baoshan	294	8.5	4.8	C	4	27	23	39	5
Jiading	464	4.0	4.8	C	6	24	18	44	5
Suburban Area									
Pudong	1430	1.9	7.0	C	9	28	14	45	3
Fengxian	720	2.4	7.2	C, N	6	10	12	64	4
Rural Area									
Chongming	1185	1.7	7.2	N	11	12	1	80	7

[a]Land use data were adopted from *Xu et al.* [2004]. Urban land included all the commercial areas, public facilities, and urban residence. Green land was designated the coverage of public and residential parks, roadside shade trees, and natural vegetation.
[b]River network density and channel storage data were adopted from *Yuan and Yang* [2011].
[c]"N" and "C" denote natural and concreted riverbank types, respectively.

The Shanghai river network is the downstream portion of a lake-rich landscape, receiving over 80% of its runoff from the Taihu Lake [*Yin et al.*, 2013] (Figure 1). The river network is extremely dense and has a total water area of 570 km^2, equivalent to about 9% of Shanghai's total terrain. The Huangpu River (300–700 m width and 9–17 m depth), the last tributary of the Yangtze River, is the backbone of the river network (Figure 1). Most rivers in the Shanghai river network are influenced by diurnal tidal cycle and feature a hydrological stagnation, characterized by a sluggish and bidirectional flow velocity, especially during the dry season (November to February) [*Yin et al.*, 2013]. During the flooding season (July and August), however, the water table and discharge of the river network are dramatically increased by flooding waters from the Taihu Lake basin [*Yin et al.*, 2013]. The mean annual net discharge of the Huangpu River measured at the Mishidu Gauge Station (the starting point of Huangpu River's main stem; Figure 1) was 1.07×10^{10} m^3 yr^{-1} (339 m^3 s^{-1}) toward the Wusong Mouth (Figure 1) (Shanghai Water Bureau, 2011, http://www.shanghai-water.gov.cn/swEng/index.jsp, accessed 10 May 2016).

2.2. Delineation of River Network and Sampling Areas

The Landsat-7 ETM+ images in 2009 (30 m pixel) and an aerial remote-sensing image of Shanghai in 2008 (1 m pixel) were used to delineate the river network using the ArcGIS 9.2 software [*Yu et al.*, 2013]. The geospatial layer of the river network was extracted and rasterized into 1 m^2 unit blocks for calculating river geometry and spatial extrapolation of CO_2 and CH_4 evasions (see below). We divided the Shanghai river network into four areas, that is, headwater, urban, suburban, and rural areas, based on river hydromorphological properties and watershed land use of the 10 administrative districts of the Shanghai City (Figure 1). The river hydromorphology and watershed land use data were adopted from *Yuan and Yang* [2011] and *Xu et al.* [2004], respectively (Table 1). The headwater area encompassed the source regions of the river network downstream the lakes. The channel geomorphology of the headwater rivers received the least human disturbances, featuring high bifurcation ratio and channel storage [*Yin et al.*, 2013]. The land use of this area consisted of more than half of agricultural land and about 15% of urban land. Therefore, the definition of "headwater river" in this study is different from what is sometime referred to as first-order streams draining undisturbed landscapes. The suburban rivers were mostly straight artificial canals for agricultural and transportation uses. The districts in the suburban area served multiple municipal functions, including considerable agricultural land (≥45%) and scattered urban and industrial coverage. The urban area was characterized by dominant urban and industrial land use (58%) and encompassed the middle and lower reaches of the Huangpu River. The urban rivers were subject to the most intensive human alterations, featuring an extremely low bifurcation ratio. Moreover, effluents of municipal wastewater treatment plants (WWTPs) serving the Shanghai City were mostly discharged into the urban rivers [*Yu et al.*, 2013]. Finally, the Chongming

Island, dominated by agricultural land use (80%), was designated as the rural area. Notably, riverbank properties differed evidently among the four areas (Table 1), with nearly all the urban and suburban rivers having concreted riverbanks in support of flooding control (Figure S2).

2.3. River Order Designation and Sampling Sites

The Shanghai river network has a reticular structure with hierarchical drainage loops (Figure 1). This structure is a result of both reduced erosional forces in the deltaic deposition environment and anthropogenic alterations [*Zhao et al.*, 2015]. For example, many rivers in the Shanghai downtown area were buried for integrated urban constructions, while artificial canals were constructed in the southeastern corner to ease agricultural water use. Consequently, the Horton-Strahler stream ordering law is not readily applicable to delineating stream order or subwatershed boundaries in this river network. *Mileyko et al.* [2012] proposed that in planar reticular networks width is the best weighting factor to generalize the Horton-Strahler ordering scheme. Therefore, we adopted the river width (w) versus stream order (ω) relationship (equation (1)) derived by *Downing et al.* [2012] using a global stream and river data set to calculate the river order for each surveyed river.

$$\omega = 1.214^{*}\ln^{1.845w} \tag{1}$$

Using the rasterized geospatial layer (1 m pixel) of the river network and the "Calculate Geometry" and "Collapse Dual Lines To Centerline" functions of ArcGIS 9.2 software, we calculated river length and mean river width for the delineated rivers. We then divided the total river areal area into three river width categories: (1) less than 10 m, (2) greater than 10 m and less than 100 m, and (3) greater than 100 m. The results show that rivers within these three categories composed 2% (<10 m wide), 82% (>10 m and <100 m wide), and 16% (>100 m wide) of the total river areal area, respectively, indicating that most rivers within the Shanghai river network were of fourth to sixth order as calculated using equation (1).

Therefore, we set 4 to 15 sampling sites in each administrative district based on the spatial distributions of river network density (i.e., river areal area per surface area) and river order. This resulted in 87 sampling sites that resolve local structure of the reticular drainage systems (i.e., no more than one sampling site on a same river reach) (Figure 1 and Table 1). All the inlets (headwater tributaries of the Huangpu River) and outlet (Wusong Mouth) of the river network were covered by this sampling design. In addition, four sites were longitudinally set along the main stem of the Huangpu River (Figure 1). The mean river width of the sampled rivers ranged between 9 m and 531 m (first-third quartile: 21–65 m), corresponding to river order from fourth to eighth order (first-third quartile: fourth – sixth order) (Figure S3). Notably, the urban and suburban areas were dominated by lower order rivers (i.e., fourth to fifth; Figure S3).

2.4. Sampling Methods

Thirteen sampling campaigns were conducted, spanning a 27 month period. The first two campaigns were conducted in August and December 2009, respectively, and the rest ones were conducted bimonthly from February 2010 to October 2011. The rural rivers were not sampled in the first two campaigns. During each sampling visit, triplicate surface water samples (~15 cm below water surface) were sampled using a Van Dorn sampler for the $p\text{CO}_2$ and $p\text{CH}_4$ measurements (see below). Two 180 mL atmospheric gas samples were collected and injected into prevacuumed gas bags using syringes equipped with a three-way valve. In situ water temperature and salinity (YSI 30; precision and accuracy of salinity measurement = 0.1 ppt), pH (Spectrum IQ 150), and dissolved oxygen (DO) concentration (Myratek Sentry M-2; precision and accuracy = 0.01 mg L^{-1}) were measured in surface water by calibrated portable instruments. DO saturation was calculated using an oxygen solubility constant corrected by in situ water temperature [*Weiss*, 1970] and an assumed atmospheric oxygen concentration of 0.21 atm. The pH measurements were calibrated by three National Bureau of Standards pH buffers (pH = 4.01, 7.00, and 10.01) and had a precision and accuracy of 0.03 pH unit. Additional 150 mL of surface water sample was collected for NH_4^+ and nitrate (NO_3^-) concentration measurements using standard colorimetric methods on a continuous flow injector. Water samples collected during February 2010 to December 2010 were also analyzed for sulfate (SO_4^{2-}) concentration using the continuous flow injector. All the water samples were acquired during daytime, stored under ice, shielded from sunlight, and transported to the laboratory within 6 h.

2.5. Surface Water $p\text{CO}_2$ and $p\text{CH}_4$

Surface water $p\text{CO}_2$ and $p\text{CH}_4$ were measured using a headspace equilibration method that has been described for N$_2$O saturation measurements by *Yu et al.* [2013]. In brief, a 140 mL gas-tight water sampling

tube was overflowed for two to three volume changes using water released from the Von Dorn sampler. Then, the tube was quickly stoppered by a halobutyl rubber septa using an open-topped screw cap, excluding any air bubbles. About 0.2 mL of saturated mercuric chloride solution was injected through the septa to poison the sample. Back in the laboratory, a 60 mL headspace was created by injecting ultrapure N_2 (>99.999%) to the sampling tube, while simultaneously drawing out 60 mL of the sample water. The tube was then shaken vigorously for 5 min and left for 30 min at room temperature to equilibrate. Ten milliliter of the equilibrated headspace air was then extracted and injected into a gas chromatograph with a flame ionization detector (Agilent 7890A) to determine its CO_2 and CH_4 concentrations. Three gas standards (10,000 ppm CO_2 and 200 ppm CH_4, 1000 ppm CO_2 and 20 ppm CH_4, and 300 ppm CO_2 and 2 ppm CH_4) were used for concentration calibration. Repeated measurements using the standards indicated that precision of the CH_4 and CO_2 analysis are within ±0.12% and ±0.10% of expected concentrations in parts per million, respectively. The original surface water pCO_2 was then calculated based on the volume ratio of headspace to water in the sampling tube and a temperature-corrected CO_2 solubility constant [*Weiss*, 1974] (details are provided in the supporting information). A similar procedure employing a CH_4 solubility constant [*Wiesenburg and Guinasso*, 1979] was used for pCH_4 calculation.

2.6. Air-Water CO_2 and CH_4 Fluxes

Air-water CO_2 and CH_4 fluxes (fCO_2 and fCH_4) were estimated using a two-layer model that describes diffusive gas exchange as driven by the pressure gradient and the gas transfer velocity (k) across the air-water interface:

$$fC = k\alpha(pC_{water} - pC_{atm}) \tag{2}$$

where fC is the air-water flux, α is the gas solubility constant, ($pC_{water} - pC_{atm}$) is the partial pressure gradient at the air-water interface, and k is the gas transfer velocity across the air-water interface. The gas transfer velocity of CO_2 (k_{CO2}) and CH_4 (k_{CH4}) was estimated using normalized k corresponding to k_{CO2} at 20°C (k_{600}), in situ water temperature, and Schmidt number scaling [*Jähne et al.*, 1987]:

$$k_{CO2} = k_{600} * \left(\frac{Sc_{CO2}}{600}\right)^{-n} \tag{3}$$

In equation (3), n is a proportionality coefficient that describes the turbulent nature of water surface. We chose n to be 0.5 to represent a moderately turbulent surface in low-gradient, high-order rivers [*Alin et al.*, 2011; *Beaulieu et al.*, 2012; *Campeau et al.*, 2014; *Abril et al.*, 2014]. The k_{CH4} was calculated from equation (3) using the temperature-dependent Schmidt number of CH_4 [*Jähne et al.*, 1987].

Despite numerous studies on the subject, important uncertainty remains regarding the parameterization of k_{600} in surface water systems where turbulence can be controlled by both water currents and winds [*Alin et al.*, 2011; *Beaulieu et al.*, 2012]. While both driving forces can be individually modeled with reasonable accuracy [*Borges et al.*, 2004; *Beaulieu et al.*, 2012], it is extremely difficult to depict turbulence regime of the Shanghai river network at the watershed scale due to its heterogeneous and complex nature. For example, the mean river width of the studied rivers, a surrogate for river surface area, ranges from 9 m to 531 m, suggesting variable potential for wind to generate turbulence across the river network; water velocity could vary over a wide range (e.g., 0–1 m s^{-1}) within the river network due to multiple factors, including tidal cycle, flooding, and dam impoundment. However, we expect greater contribution of wind-induced turbulence to gas exchange in the Shanghai river network than in other less-managed river systems because (1) turbulence created from shear friction at the riverbed is limited by the low channel slopes in this deltaic depositional system [*Raymond and Cole*, 2001] and (2) channel straightening and embankment of the urban and suburban rivers may diminish fetch limitation (e.g., interruption of wind blows over water surface), leading to greater wind stress, wave breaking, and enhanced k_{600} at any given wind speed [*Borges et al.*, 2004]. Applying the widely used hydraulic geometry scaling law proposed by *Raymond et al.* [2012] to the main stem of the Huangpu River (500 m width, 10 m depth, and slope < 0.04‰ [*Yin et al.*, 2013]) results in erroneously large discharge (>6000 m^3 s^{-1}), indicating that hydraulic geometry-based turbulence models calibrated for headwater streams and small rivers [e.g., *Raymond et al.* [2012]] are not applicable to modeling k_{600} of this lowland coastal river network [*Rasera et al.*, 2013].

In this study, we calculate k_{600} using six different predictive models developed for low-gradient large rivers and estuaries. These models scale k_{600} with wind speed at 10 m above water surface (U_{10}) and are based
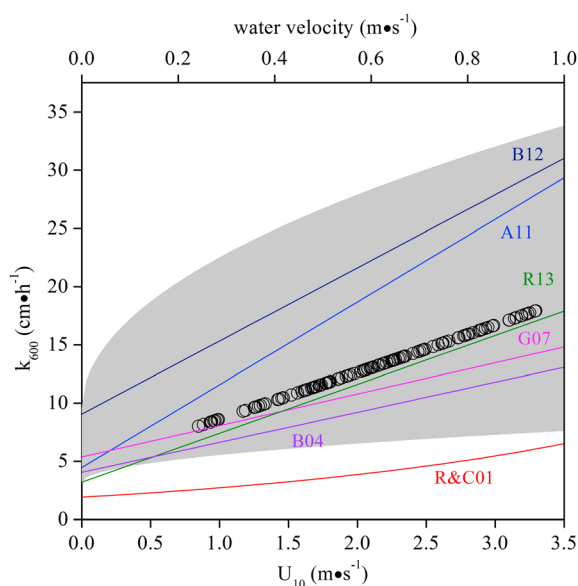
Figure 3. Comparison of k_{600} parameterizations as a function of U_{10}. Abbreviations: R&C01-*Raymond and Cole* [2001], B04-*Beaulieu et al.* [2012], G07-*Guérin et al.* [2007], A11-*Alin et al.* [2011], B12-*Beaulieu et al.* [2012], R13-*Rasera et al.* [2013]. Detailed information regarding each parameterization is provided in Table S2. Average k_{600} values (open dots) based on all the six parameterizations are used for $f CO_2$ and $f CH_4$ flux calculations. The shaded area denotes the range of synthetically generated k_{600} using equation (4) as a function of water velocity.

on direct k_{600} measurements under hydrological (e.g., water velocity) and meteorological conditions (e.g., wind speed) similar to those of the Shanghai river network. The k_{600} parameterization of these models is summarized in Figure 3 and described in more detail in Table S2. Importantly, water current as a major driver of turbulence at the water-air interface is implicitly accounted for in all these models, as illustrated by the nonzero k_{600} values at zero wind speed (Figure 3). Hourly averaged U_{10} data for each district were collected from the website of Shanghai Meteorological Bureau during the entire study period. These data were then used to calculate monthly average wind speed for k_{600} calculations.

To further evaluate whether water current-induced turbulence is adequately represented in the wind-based k_{600} parameterizations, the wind-based k_{600} parameterizations were compared with a group of synthetic k_{600} generated from a composite model that explicitly addresses both wind- and water current-induced turbulence [*Borges et al.*, 2004]. This composite model uses instantaneous water velocity (v), river depth (D), and U_{10} to model k_{600} (equation (4)) and has been proven effective in providing representative k_{600} estimates for large rivers and estuaries [*Borges et al.*, 2004; *Beaulieu et al.*, 2012].

$$k_{600} = 17.19 v^{0.5} D^{-0.5} + 2.58 \times U_{10} + 1.0 \qquad (4)$$

Using typical v (0.01–1 m s^{-1}), D (0.5–15 m), and U_{10} (0.8–3.3 m·s^{-1}) of the Shanghai river network, the composite model predicts k_{600} ranging between 3.2 cm h^{-1} and 33.8 cm h^{-1} (shaded area in Figure 3). This range is generally consistent with the wind-based k_{600} parameterizations over the same range of wind speed, except *Raymond and Cole*'s [2001] empirical model which predicts lower k_{600} (1.9–7.7 cm h^{-1}) (Figure 3). Therefore, for each flux calculation, we used an average k_{600} value based on all the six models and consider it as a conservative way to estimate $f CO_2$ and $f CH_4$.

2.7. Segment-Scale CO$_2$ Source Partitioning

Riverine CO_2 oversaturation and subsequent CO_2 emissions are primarily driven by internal metabolic CO_2 production (hereafter "internal production") as well as external hydrological inputs of DIC through upstream runoff (hereafter "longitudinal input") and lateral groundwater fluxes (hereafter "lateral input") at segment scales (Figure S1) [*Abril et al.*, 2014; *Gómez-Gener et al.*, 2016]. In this study, a dynamically coupled DIC-CO_2-O_2 model [*Gómez-Gener et al.*, 2016; *Stets et al.*, 2017] was used to quantify and differentiate the relative contribution of these sources to the measured pCO_2 and CO_2 evasion along the longitudinal transect of the Huangpu river (Figure 1). Lateral surface water inputs to this transect (e.g., tributaries or sewage discharges) were small (<2% of the net annual mean discharge) (Shanghai Water Bureau, 2011, http://www.shanghai-water.gov.cn/swEng/index.jsp, accessed 10 May 2016). The coupled DIC-CO_2-O_2 model is essentially a one-dimensional transport model that calculates theoretical downstream CO_2 concentration through iterative simulation of CO_2 addition or removal via gas exchange and internal production [*Abril et al.*, 2014]. Moreover, in the Shanghai river network, a first-order estimate on the carbonate system based on the measured pH (site-averaged pH: 7.5 ± 0.2) and pCO_2 (see below) indicates that bicarbonate ion (HCO$_3^-$)

constituted more than 75% of the DIC pool at all the study sites [*Millero*, 2007]. The aqueous carbonate equilibrium is therefore included in the model to account for the carbonate buffering effect on dissolved CO_2 dynamics [*Stets et al.*, 2017].

The model simulation starts from the Mishidu Gauge Station (Figure 1). During each model iteration, the distance (Δx) (m) traveled by the water mass over each model time step (Δt) is calculated using water velocity (v; m s^{-1}):

$$\Delta x = v\Delta t \tag{5}$$

Changes in DIC concentration between position x and $x + \Delta x$ are simulated by accounting for gas exchange, internal production, and reequilibration of the DIC pool:

$$DIC_{(x+\Delta x)} = DIC_{(x)} - \left[k_{CO2}\alpha_{CO2}\left(pCO_{2(x)} - pCO_{2(atm)}\right) - IP_{(x)} \right] \times \frac{\Delta t}{D} \tag{6}$$

where IP is the internal production of CO_2 (g C m^{-2} d^{-1}) and D is the mean river depth (m). We assumed that alkalinity is a conservative quantity during the transport, since the loss or addition of dissolved CO_2 does not change the charge balance of the system [*Stets et al.*, 2017]. The $pCO_{2(x + \Delta x)}$ can therefore be calculated from $DIC_{(x + \Delta x)}$ and initial alkalinity at each time step (details and equations are provided in the supporting information). In the model, IP is estimated using DO dynamics along the transect [*Hotchkiss et al.*, 2015; *Gómez-Gener et al.*, 2016]. The governing equation for DO dynamics is given by

$$DO_{(x+\Delta x)} = DO_{(x)} + \left[k_{O2}\left(DO_{(x)} - DO_{(atm)}\right) + NEP_{(x)} \right] \times \frac{\Delta t}{D} \tag{7}$$

where k_{O2} is the specific gas transfer velocity for O_2, $DO_{(atm)}$ is the saturated DO concentration in atmospheric equilibrium (mM), and NEP is the aquatic net ecosystem production (mmol O_2 m^{-2} d^{-1}). The k_{O2} was obtained from k_{CO2} by applying equation (3). NEP at each time step is estimated by fitting equation (7)) to longitudinal profile of DO along the transect and then converted to IP by assuming the CO_2:O_2 stoichiometry of aerobic respiration equal to 1 [*Hotchkiss et al.*, 2015; *Stets et al.*, 2017]. Aquatic metabolism contributes to CO_2 oversaturation when NEP is negative, that is, when ER is greater than GPP due to aquatic mineralization of allochthonous OC.

We ran the coupled DIC-CO_2-O_2 model to simulate pCO_2 along the transect on an annual scale under two scenarios. Scenario 1 assumes no internal CO_2 production (i.e., IP fixed at zero in equation (6)) and is aimed at exploring potential extent of pCO_2 that can be maintained by longitudinal input alone without the necessity of internal production or lateral input (see Figure S4 for an illustration). In scenario 2, internal production is allowed to replenish the DIC pool. Therefore, difference in the simulated pCO_2 between the two scenarios reflects the relative importance of internal production (Figure S4). Furthermore, the relative role of lateral input in sustaining pCO_2 and CO_2 emissions can be assessed by comparing the simulated pCO_2 under scenario 2 with the measured pCO_2 along the transect (Figure S4).

For model implementation under both scenarios, the model iteration time was set at 1 min. The initial DIC concentration and alkalinity were estimated using annual average pH and pCO_2 measured at the Mishidu Gauge Station, assuming that contribution of organic acids to alkalinity was negligible (more details and discussion are provided in the supporting information). To estimate NEP, longitudinal DO profile was interpolated using annual DO concentrations measured at the four sites along the transect. Instead of using instantaneous water velocity, water velocity (0.07 m s^{-1}) calculated from the net annual mean discharge (339 m^3 s^{-1}) and mean river cross section of the Huangpu River (5000 m^2) was used in the model to account for the tide-induced bidirectional flow regime and thus to represent net downstream transport of water and CO_2. As can be seen in equations (6) and (7), k_{CO2} and k_{O2} are important model parameters that determine how fast the dissolved CO_2 and O_2 are lost or replenished via the air-water exchange relative to downstream movement of the water currents (i.e., 0.07 m s^{-1}). We used three different k_{600} values for calculating k_{CO2} and k_{O2} to account for the uncertainty in our k_{600} parameterization (see above). These three k_{600} values was calculated as the average and average plus and minus one standard deviation using the six wind-based k_{600} models (Figure 3) and annual average U_{10} of the four longitudinal sampling sites. Finally, we used a graphical method to interpret the simulated pCO_2 and partition the relative contribution of the major CO_2 sources. As illustrated in Figure S4, areas under and between the simulated and measured curves of pCO_2

in excess to the atmospheric $p\text{CO}_2$ were integrated using the *trapz* function in MATLAB (Mathworks, Natick, MA, USA). The fractional contributions of longitudinal input and internal production were calculated as the ratio of the respectively simulated $p\text{CO}_2$ area to the total area defined by the measured $p\text{CO}_2$ (Figure S4). The fractional contribution of lateral input was then calculated by subtraction (Figure S4).

2.8. Annual CO_2 and CH_4 Evasion

A spatial extrapolation technique was used to calculate the annual CO_2 and CH_4 evasion from the Shanghai river network [*Yu et al.*, 2013]. The $f\text{CO}_2$ and $f\text{CH}_4$ estimated for each study site were first extrapolated into the entire administrative territory of Shanghai using the Kriging method in ArcGIS 9.2 software. The rasterized geospatial layer (1 m pixel) of the river network was then extracted; $f\text{CO}_2$ and $f\text{CH}_4$ in each pixel were identified and summed to calculate the annual evasion. The annual average $f\text{CO}_2$ and its corresponding 95% confidence intervals of each sampling site were used for the extrapolation. Because the frequency distribution of $f\text{CH}_4$ measured at most sampling sites was highly skewed (see below), median values, instead of average, were used for the extrapolation. It is important to note that the inability of this extrapolation method to account for presumably higher emissions in small streams within the Shanghai river network (i.e., rivers <10 m; see above) may potentially bias the annual estimates low. To ease comparisons among different ecosystems in regional C budget, the total CO_2 and CH_4 evasion from the Shanghai river network were expressed as CO_2 equivalents (CO_2-eq) by assuming that CH_4 has warming potential for a 100 year time period 25 times higher than CO_2 [*IPCC*, 2007].

2.9. Statistical Analyses

All measured variables were checked for normality using the Shapiro-Wilk's test and, when needed, were log transformed to meet the assumptions of normality and homoscedasticity. The nonparametric Kruskal-Wallis test coupled with a pairwise comparison was used to assess whether $p\text{CO}_2$ and $p\text{CH}_4$ from different areas or river order clusters were significantly different. Linear and exponential regressions and the Pearson's correlation were used to detect relationships between independent variables. Causal relationships between $p\text{CO}_2$ and $p\text{CH}_4$ and the watershed land use were explored using stepwise multiple linear regression (MLR) and principal component analysis (PCA). The land use percentage (i.e., percentage of urban, industrial, agricultural, and vegetated lands) and the river density of each district (Table 1) were assigned to every sampling sites within the same district. The criteria for inclusion used in the MLR were F to enter >4 and F to remove <3.95. In the PCA, the Kaiser-Meyer-Olkin and Bartlett's sphericity tests were used to measure the appropriateness of the data for PCA; varimax rotation with the Kaiser normalization was used to obtain rotated component matrix. All the statistical tests were performed using SPSS 17.0 (SPSS Inc., Chicago, IL, USA).

3. Results

Due to distinct seasonality of the measured $p\text{CO}_2$ and $p\text{CH}_4$ (see below) and the temporally uneven sampling design (e.g., three August sampling campaigns versus two campaigns in all the other sampling months), the measured $p\text{CO}_2$, $p\text{CH}_4$, and water chemistry variables were grouped by month to calculate monthly averages, which were then used for calculation of annual averages or median values at various spatial scales. The complete data sets of annual averages (or median values in the case of $p\text{CH}_4$ and $f\text{CH}_4$) of the measured gas partial pressures, evasion rates, and water chemistry variables can be found in Tables S3 and S4. All the measured $p\text{CO}_2$ and $p\text{CH}_4$ of individual samplings are shown in Figures S5 and S6.

3.1. Spatial and Temporal Variations of Water Chemistry Variables

The general spatiotemporal variations of the measured water chemistry variables have been reported in *Yu et al.* [2013] (Figure S7 and Tables S5–S8). Here we focus on patterns closely related to the $p\text{CO}_2$ and $p\text{CH}_4$ dynamics. DO deficiency was throughout the river network, with the area-averaged DO saturation ranging from $31.2 \pm 13.2\%$ to $67.0 \pm 10.5\%$. The urban rivers had the lowest DO saturation and frequently experienced hypoxia (DO < 2 mg L^{-1}) (Figure S7a). The pH of the mainland rivers (i.e., rivers in the headwater, suburban, and urban areas) was generally between 7.0 and 8.0 with lower pH occurring during the dry season (Figure S7b). NH_4^+ and NO_3^- concentrations were significantly higher in the mainland river network than the rural rivers (Figures S7e and S7f). The fourth and fifth-order rivers in the urban area had the highest NH_4^+ concentrations (up to 12 mg N L^{-1}). The monthly averaged DO saturation, salinity, NH_4^+, NO_3^-, and
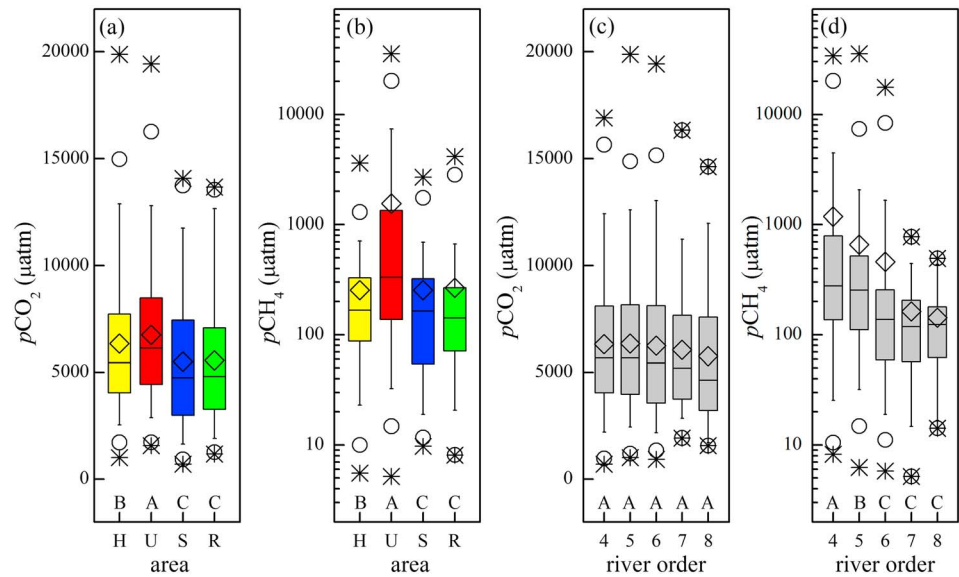
Figure 4. River pCO_2 and pCH_4 by the (a and b) four areas and (c and d) river order. The rural rivers were not included in Figures 4c and 4d. The box extent, line inside the box, and error bars denote 25th and 75th, 50th, 10th, and 90th percentiles, respectively. Arithmetic mean, 5th and 95th, and maximum and minimum values are displayed by the diamonds, cycles, and asterisks, respectively. Letters "H," "U," "S," and "R" represent the headwater, urban, suburban, and rural rivers, respectively. The letters below the boxes denote significant differences determined by pairwise Kruskal-Wallis test.

SO_4^{2-} in the four areas were all negatively correlated with water temperature (3.8°C to 33.3°C; $P < 0.05$ in all the cases; Figure S7) and precipitation ($P < 0.05$ in all the cases). Significant positive correlations ($P < 0.05$ in all the cases; Tables S5–S8) between pH and DO saturation were also detected in the four areas.

3.2. Spatial and Temporal Variations of pCO_2 and pCH_4

pCO_2 in the urban rivers ranged from 1572 to 19425 μatm, 6521 ± 2628 μatm on average, and was significantly higher than in the headwater (6117 ± 2812 μatm, $P < 0.05$), suburban (5091 ± 2764 μatm, $P < 0.01$), and rural (5076 ± 2602 μatm, $P < 0.01$) rivers (Figure 4a). Although extremely highly pCO_2 (e.g., >15,000 μatm) was occasionally measured in the urban and headwater rivers (Figure 4a), pCO_2 pooled over the entire river network were normally distributed for each sampling month (Figure S5). No significant difference in pCO_2 was found between the rivers in different orders in the mainland river network ($P > 0.05$ in all the comparisons; Figure 4c). An evident positive relationship was found between water temperature and the monthly averaged pCO_2 in the four areas (Figure 5a). The temperature quotient (Q_{10}) calculated using an exponential fit ranged from 1.48 to 1.61 for the four areas (Figure 5a).

The frequency distribution of the measured pCH_4 was positively skewed (Figures 4b and 4d and S6). pCH_4 in the urban rivers varied over 4 orders of magnitude over the entire study period (5.2 μatm to 35,274 μatm, median 585 μatm) and was significantly higher than in the headwater (median 193 μatm), suburban (median 169 μatm), and rural (median 143 μatm) rivers ($P < 0.01$ in all the comparison; Figure 4b). pCH_4 in the fourth and fifth-order rivers were significantly higher than in the higher-order rivers (Figure 4d). No clear pattern was emerged in the relationships between pCH_4 and water temperature (Figure 5b). However, pCH_4 in the urban rivers were significantly higher during the dry season than during the wet season ($P < 0.01$).

3.3. Relationships Between pCO_2 and pCH_4, Water Chemistry Variables, and Land use

DO saturation, pH, and salinity were all negatively correlated with pCO_2 in the four areas ($P < 0.05$ in all the cases; Tables S4–S7). DO departure from saturation and CO_2 excess from saturation were plotted by month for the four areas in Figure 6. While a negative correlation between CO_2 excess and DO departure was evident over the entire study period, disproportionally increased CO_2 excess relative to DO departure was recorded during the flooding season (i.e., August) (Figure 6). The MLR resolved more than 65% of variance in pCO_2, and the results suggest that water temperature and DO saturation were the most powerful predictors of pCO_2 for the entire river network (Table 2). The pH, NH_4^+, and salinity were included in the MLR in three of the four areas,
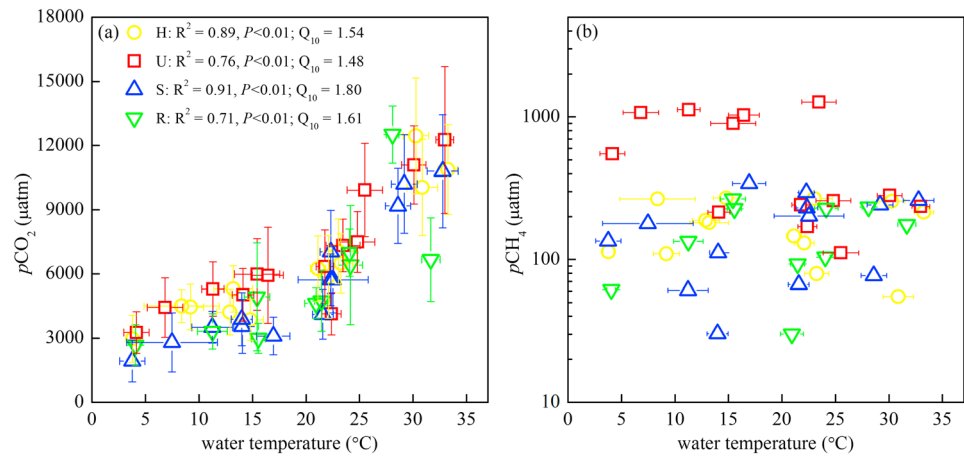
Figure 5. (a) Monthly average of pCO_2 and (b) monthly median value of pCH_4 as a function of water temperature. The error bars denote one standard deviation (1σ). Letters H, U, S, and R represent the headwater, urban, suburban, and rural rivers, respectively. R^2 of exponential fit and Q_{10} of the relationship between pCO_2 and water temperature are shown in the legend.

while the percentage land use was only included in the MLR model for the suburban area (Table 2). The first two components of the PCA (PC1 and PC2) illustrate key relationships among the variables pooled over the entire river network by month and resolved 45% to 51% of variance in the variables (Figure 7). In April and December, pCO_2 was highly correlated with PC1 that consisted of the percentage land use, NH_4^+, and DO saturation (referred to as the land use component hereafter) and weakly correlated with PC2 that consisted of salinity, NO_3^-, river order, and river density (referred to as the salt-geomorphology component). In June, August, and October, pCO_2, pH, and river density constituted an independent principal component orthogonal to the land use component. In February when the lowest water temperature was recorded, pCO_2 was modestly correlated to both the land-use and the salt-geomorphology components (Figure 7).

pCH_4 was negatively correlated with DO saturation in the mainland river network ($P < 0.05$ in all the cases; Tables S5–S8). Significant positive correlations between pCH_4 and NH_4^+ were also found in the urban and
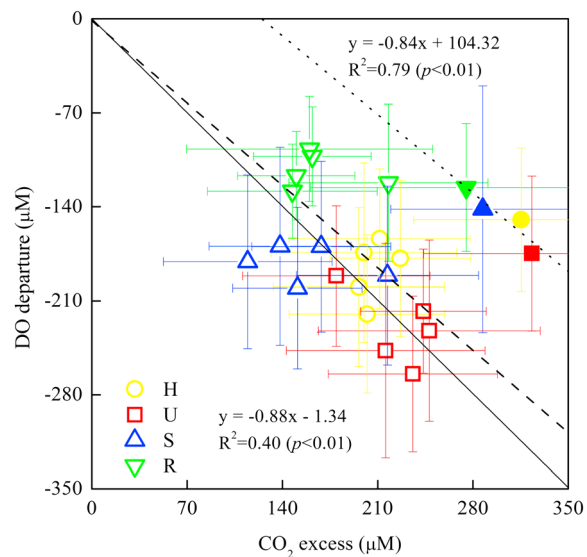

Figure 6. Relationship between DO departure from saturation and CO_2 departure from saturation for each sampling month. Letters H, U, S, and R represent the headwater, urban, suburban, and rural rivers, respectively. Data collected in the same month but different years were grouped and averaged. The error bars denote one standard deviation (1σ) of the calculated average values. The filled symbols are for the flooding season (August). The solid line shows the 1:1 slope line. The dotted and dashed lines are the linear regression fits of the August data and the data pooled over all the other sampling months, respectively.

Table 2. Stepwise Multiple Regression Analysis of pCO_2 and pCH_4 Using Independent Variables Depicting Water Chemistry, Land Use, and River Geomorphology of the Four Areas[a]

Independent Variable	R^2 (Adj.)	Independent Variable	R^2 (Adj.)	Independent Variable	R^2 (Adj.)	Independent Variable	R^2 (Adj.)
Headwater pCO_2		Urban pCO_2		Suburban pCO_2		Rural pCO_2	
Temperature (+)***	0.61	Temperature (+)***	0.66	Temperature (+)***	0.51	Temperature (+)***	0.45
pH (−)***	0.72	DO (−)***	0.73	Ln[DO%] (−)***	0.61	DO (−)***	0.64
DO (−)***	0.76	Ln[NH_4^+] (+)***	0.76	pH (−)***	0.64	Ln[Salinity] (−)*	0.65
Ln[NH_4^+] (+)***	0.77	pH (−)***	0.78	Ln[NH_4^+] (+)***	0.68		
Salinity (−)*	0.78	Salinity (−)***	0.79	Urban% (−)*	0.72		
Independent Variable	**R^2 (Adj.)**	**Independent Variable**	**R^2 (adj.)**	**Independent Variable**	**R^2 (adj.)**	**Independent Variable**	**R^2 (adj.)**
Headwater pCH_4		Urban pCH_4		Suburban pCH_4		Rural pCH_4	
River order (−)***	0.07	Ln[NH_4^+] (+)***	0.22	River order (−)**	0.05	Ln[NH_4^+] (+)*	0.07
pH (−)**	0.11	pH (−)***	0.34	Ln[NO_3^-] (−)**	0.10	pH (−)*	0.15
Industry%**	0.13	Agriculture% (−)***	0.39	pH (−)**	0.14		
Ln[NO_3^-] (−)*	0.14	River density (+)***	0.44	Urban% (−)*	0.16		
		River order (−)**	0.46				
		Ln[NO_3^-] (−)*	0.46				

[a]Log normally distributed variables are log-transformed before entering into the models. For each model, final set of predictors is shown in order of inclusion. "Plus" and "minus" signs in the brackets denote positive and negative relationships between predictor and gas partial pressures, respectively. Statistical significance of each step of predictor inclusion is indicated by the asterisks with "*," "**," and "***" denoting $P < 0.05$, $P < 0.01$, and $P < 0.001$, respectively.

rural areas ($P < 0.01$ in both cases; Tables S5 and S7). In the MLR, the percentage land use and river order were generally better predictors of pCH_4 than the water chemistry variables in the mainland river network (Table 2). The PCA results indicated a consistent correlation between pCH_4 and the land use component in all the sampling months (Figure 7).

3.4. Longitudinal pCO_2 Dynamics and CO_2 Source Partitioning

The measured pCO_2 and DO saturation were not significantly different between the four longitudinal sampling sites of the Huangpu River on an annual basis ($P > 0.05$; Figure 8). DO saturation was consistently low along the transect, ranging from $42.3 \pm 16.2\%$ to $54.3 \pm 16.6\%$ (Figure 8a). Fitting equation (6) to a linear regression fit of the measured DO concentrations ($R^2 = 0.92$) yielded an internal CO_2 production rate of 5.00 g C m^{-2} d^{-1} (2.68–7.31 g C m^{-2} d^{-1}) along the transect (Figure 8a), within the range reported for heterotrophic streams and estuaries [*Hoellein et al.*, 2013]. Using the three different k_{600} as model input (5.8 cm h^{-1}, 11.5 cm h^{-1}, and 17.3 cm h^{-1}), the coupled DIC-CO_2-O_2 model estimated that longitudinal input, internal production, and lateral input contributed to 43% (31–65%), 44% (32–50%), and 13% (3–19%) of the measured pCO_2 and CO_2 evasion on an annual basis, respectively (Figure 8b).

3.5. Fluxes and Annual Evasion of CO_2 and CH_4

The estimated k_{600} values using the six wind-based k_{600} models ranged between 8.0 cm h^{-1} and 17.9 cm h^{-1} and was 12.7 cm h^{-1} on average for all the sampling sites (Figure 3). The annual average fCO_2 for each study site ranged from 2.92 ± 1.81 g C m^{-2} d^{-1} to 12.94 ± 3.91 g C m^{-2} d^{-1}. The annual median fCH_4 for each site ranged from 3.1 mg C m^{-2} d^{-1} to 296.6 mg C m^{-2} d^{-1}. Significantly positive linear relationships ($P < 0.01$) were found between the C gas fluxes and the partial pressures, indicating that the spatial and temporal variations of fCO_2 and fCH_4 closely tracked those for pCO_2 and pCH_4. The annual CO_2 evasion from the entire river network and the mainland rivers were 4.69 ± 2.20 Tg CO_2-eq yr^{-1} and 4.18 ± 1.94 Tg CO_2-eq yr^{-1}, respectively. The annual CH_4 evasion were 105 Gg CO_2-eq yr^{-1} and 96 Gg CO_2-eq yr^{-1} for the entire river network and the mainland rivers, respectively. An intercomparison of the C gas fluxes from different ecosystems in the Yangtze coastal region was summarized in Table 3.

4. Discussion

4.1. Biogeochemical and Hydrological Controls on River CO_2 Dynamics

In less managed drainage systems, dynamic relationships between pCO_2, water temperature, and discharge reflect how CO_2 are transported to and/or produced in streams and rivers. In upland headwater streams where CO_2 is primarily routed from near-channel soils via lateral groundwater inputs, negative correlations between pCO_2 and discharge were often observed and attributed to altered hydrologic
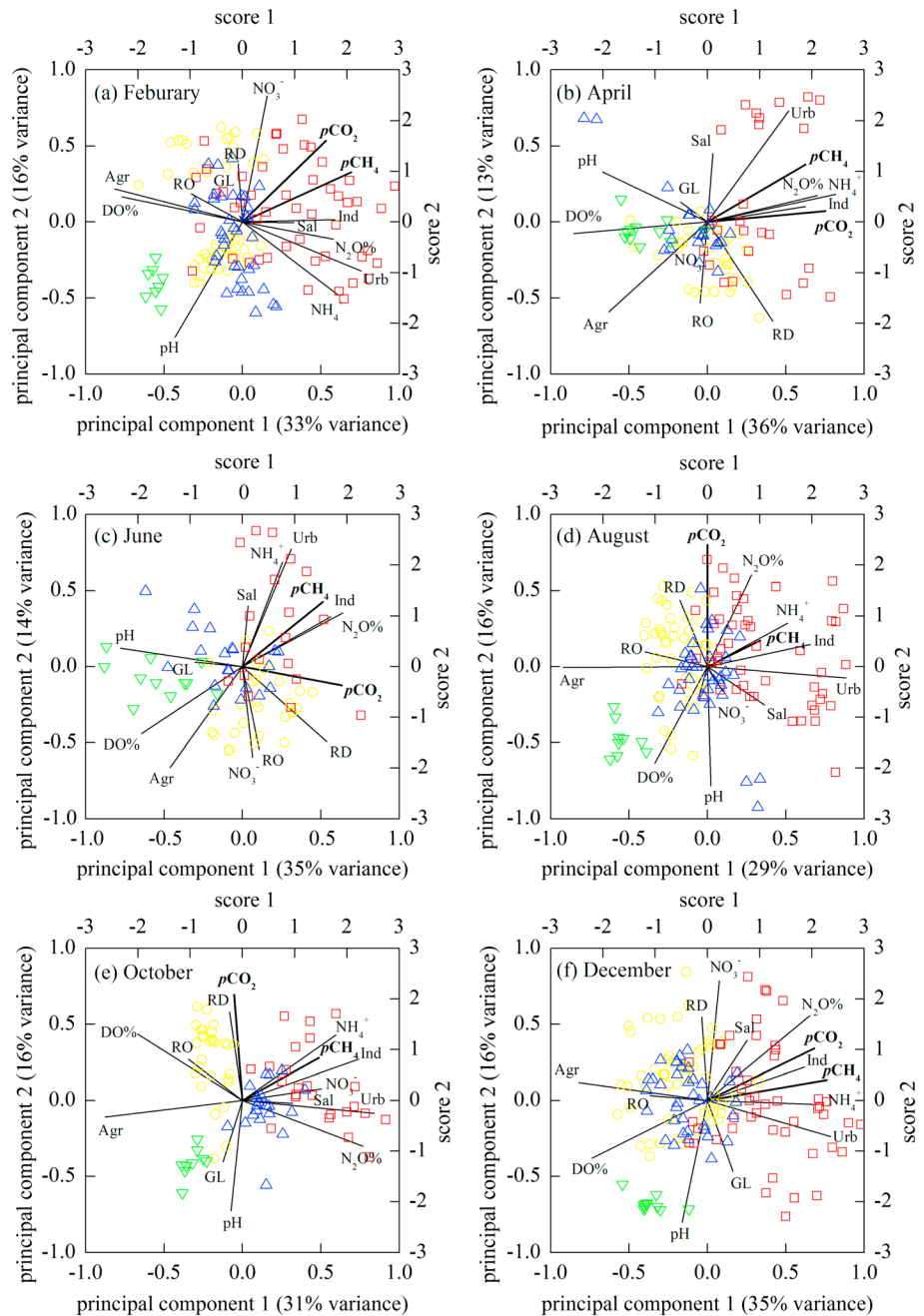
Figure 7. Principal component analysis of pCO_2 and pCH_4, land use, river geomorphology, and water chemistry variables for each sampling month. Data measured in the four areas were pooled for the analysis. The yellow, red, blue, and green dots denote the headwater, urban, suburban, and rural rivers, respectively. The percentages shown in the axis titles are the percent variance explained by the two principal components. Abbreviations: "Urb"-urban land, "Ind"-Industrial land, "Agr"-agricultural land, "GL"-vegetated land, "RD"-river density, "RO"-river order, and "Sal"-river salinity.

flowpaths during high flow events [*Johnson et al.*, 2008; *Crawford et al.*, 2013]. In contrast, discrete flooding events have been found to support a substantial fraction of CO_2 evasion via direct pumping of root respiration CO_2 from inundated fringing floodplains in lowland high-order rivers [*Abril et al.*, 2014]. Both positive and negative relationships between pCO_2 and water temperature have been observed in streams and rivers. Whereas the temperature effects on pCO_2 may be indirect, induced by, for example, enhanced soil respiration [*Öquist et al.*, 2009] or changes in the thermodynamic equilibrium of the DIC system [*Wallin et al.*, 2010], water temperature can exert formative influences on pCO_2 by controlling
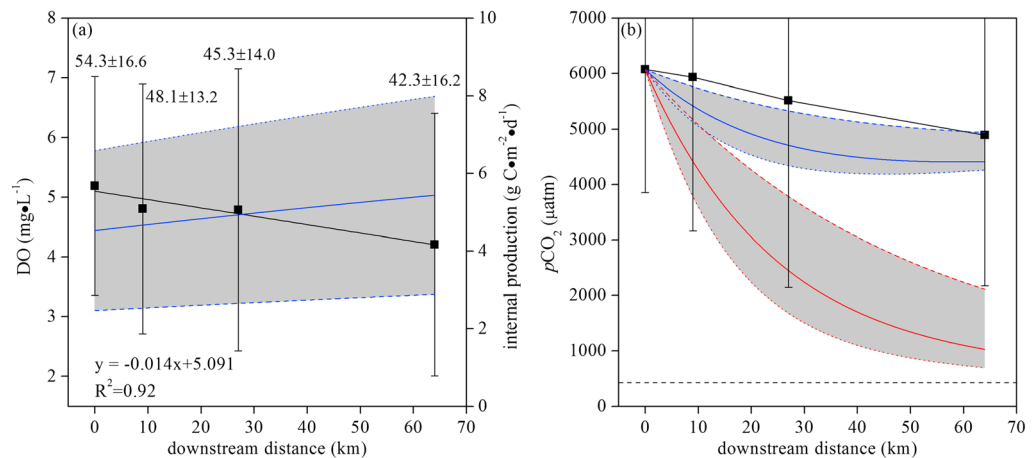
Figure 8. (a) DO dynamics and modeled internal CO_2 production along the longitudinal transect of the Huangpu River. The dots and error bars denote the annual average DO concentrations ($\pm 1\sigma$) measured at the four sites. DO saturation is also shown for each sampling site. Linear regression fit of the DO concentration data is shown as a black line. The dotted, solid, and dashed blue lines denote the modeled internal CO_2 production using three different k_{600} values, respectively (dotted—5.8 cm h^{-1}; solid—1.5 cm h^{-1}; dashed—17.3 cm h^{-1}). The shaded area denotes the uncertainty range of the modeled internal production. (b) Measured and modeled pCO_2 distribution along the longitudinal transect of the Huangpu River. The connected dots and error bars denote the annual average pCO_2 ($\pm 1\sigma$) measured at the four sites. The red and blue lines denote the modeled pCO_2 from the coupled DIC-CO_2-O_2 model adopting scenario 1 and scenario 2, respectively. The dotted, solid, and dashed blue lines denote the modeled pCO_2 under each scenario using three different k_{600} values, respectively (dotted—5.8 cm h^{-1}; solid—1.5 cm h^{-1}; dashed—17.3 cm h^{-1}). The shaded areas denote the uncertainty range of the modeled pCO_2 under the respective scenarios. The dashed horizontal line denotes the annual average of the measured ambient pCO_2 above the studied river segment (426 μatm).

aquatic metabolic CO_2 production in high-order rivers with long water residence time [*Richey et al.*, 2002; *Mayorga et al.*, 2005].

In the Shanghai river network, the rivers were CO_2-supersaturated over the entire study period (Figures 4 and 5). The measured pCO_2 (overall mean: 5846 ± 2773 μatm) is among the highest reported for high-order rivers and within the same orders of magnitude as those for the lowland Amazonian rivers (5000 ± 3300 μatm) receiving CO_2 and DOC subsidies from fringing wetlands [*Richey et al.*, 2002] and those for large Chinese urban rivers draining mountainous regions (3526 ± 3493 μatm) [*Wang et al.*, 2017] (Table S1). Recently, *Ran et al.* [2017] calculated river pCO_2 using a historical pH and alkalinity data set (1960s–1985) across the Yangtze River basin and predicted high pCO_2 (>8000 μatm) for the Taihu Lake basin. Our direct measurements confirm the widespread and persistent CO_2 supersaturation and, more importantly, reveal a dynamic correlation between pCO_2, water temperature, and discharge that has important implications for mechanistically understanding pCO_2 dynamics in human-dominated lowland coastal river networks.

Table 3. Interecosystem Comparison of CO_2 and CH_4 Fluxes

Carbon Source/Sink	Area (km^2)	Flux (g CO_2-eq m^{-2} d^{-1})	Annual Emission (Tg CO_2-eq yr^{-1})	Reference
Shanghai City				
CO_2 evasion from river network	570	10.7–47.5	4.69	This study
CH_4 evasion from river network	570	0.1–9.9	0.11	This study
Terrestrial NEP (year 2010)	6,300	2.9	−6.7	*Xu et al.* [2017]
CH_4 emission from rice fields	1,500	3.4–9.1	1.9–5.0	*Li et al.* [2005]
Taihu Lake Basin				
Terrestrial NEP (year 2010)	32,100	3.8–4.5	−53.2 to −44.7	*Xu et al.* [2017]
Estuarine Wetlands of Yangtze River				
Net CO_2 uptake	100	−4.8	−0.18	*Wang et al.* [2009]
CH_4 emissions	100	1.23	0.045	*Wang et al.* [2009]
Yangtze River Estuary (YRE) and East China Sea (ECS)				
CO_2 evasion from the YRE	7,600	1.87–6.30	1.10–2.42	*Zhai et al.* [2007]
CO_2 uptake in the river-dominated ECS	600,000	−0.22	−47.5	*Tseng et al.* [2014]
CH_4 evasion from the YRE and its adjacent marine area	203,000	0.006–0.026	0.40–0.91	*Zhang et al.* [2008]

We found multiple lines of evidence suggesting that the spatiotemporal variability of $p\text{CO}_2$ in the Shanghai river network was modulated by both biogeochemical and hydrological controls. The widespread DO deficiency (overall mean: $43.3 \pm 13.5\%$ saturation) (Figure S7a) and the negative correlations between CO_2 excess and DO departure (Figure 6) are qualitative evidence for CO_2 production via aerobic respiration. While water temperature resolved the highest variance in $p\text{CO}_2$ in the MLR models (Table 2), significant correlations were also detected between water temperature, DO saturation, and pH in the mainland river network (Tables S5–S7). Moreover, $p\text{CO}_2$ was generally higher in the urban rivers receiving nonpoint urban runoffs and WWTP effluents (Figure 4a) [*Yu et al.*, 2013], consistent with the concept that in a human-impacted aquatic system changes in DO saturation and pH are coupled to respiratory CO_2 production [*Zhai et al.*, 2007; *Noriega and Araujo*, 2014]. However, if the $p\text{CO}_2$ dynamics was only controlled by internal CO_2 production, we would expect to see temporally consistent intrasite $p\text{CO}_2$ variability with higher $p\text{CO}_2$ occurring predominately in the lower order rivers draining the urban area. In fact, no significant difference in $p\text{CO}_2$ was emerged between rivers in different order on an annual basis (Figure 4c). Persistent CO_2 supersaturation was observed in the headwater rivers (Figure 4a) and at all the network inlets (data not shown). In the PCA a consistent decoupling between $p\text{CO}_2$ and the land-use component was revealed for the wet season (Figure 7). Furthermore, the highest $p\text{CO}_2$ was recorded during the flooding season when the net river discharge reached its maximum, a condition not favorable for aquatic OC mineralization [*Johnson et al.*, 2008; *Battin et al.*, 2009]. These pieces of evidence suggest the pivotal role of external CO_2 inputs in conjunction with hydrological controls in sustaining the CO_2 supersaturation and thus evasion, in line with the results from the coupled $\text{DIC-CO}_2\text{-O}_2$ model that highlight longitudinal input and internal production as the dominant CO_2 sources (Figure 8).

Therefore, the emerged pattern of $p\text{CO}_2$ in the Shanghai river network both confirms and challenges the current conceptual understanding of river C cycling. On the one hand, our results corroborate the importance of placing river $p\text{CO}_2$ dynamics in a hydrological context for a complete examination of C fluxes along a river continuum [*Kaushal et al.*, 2014; *Gómez-Gener et al.*, 2016]. The Taihu Lake basin is an agricultural basin with high DIC concentrations ($12–30$ mg L^{-1}) in the main body of the Taihu Lake and its discharging rivers [*Tao et al.*, 2013]. The intensive agricultural activities in the rural area allow one to use the $p\text{CO}_2$ dynamics revealed for this area to infer how CO_2 was sourced upstream the studied high-order rivers. The significant correlations between $p\text{CO}_2$, water temperature, DO, and pH in the rural rivers (Table S8) suggest that mineralization of mobilized terrestrial OC might be an important source contributing to the CO_2 supersaturation in these agricultural rivers [*Butman et al.*, 2015]. More importantly, the less constrained hyporheic connectivity of the rural rivers (Table 1 and Figure S2) might favor a more efficient lateral exchange between the river channels and the adjacent terrestrial ecosystems [*Öquist et al.*, 2009; *Winterdahl et al.*, 2016]. Consequently, during high-flow events, rising of near-river water tables could intersect more emergent vegetation horizons and flush out more CO_2-rich water previously stored in riparian soils and wetlands [*Johnson et al.*, 2008], leading to enhanced longitudinal pathway of CO_2 supply along the river network [*Abril et al.*, 2014; *Gómez-Gener et al.*, 2016]. This pulse-like CO_2 input to the upstream rivers together with reduced water residence time and the buffered CO_2 equilibrium [*Stets et al.*, 2017] might collectively result in the spatially homogeneous $p\text{CO}_2$ (Figure 4c), the "anomalous" CO_2 excess (Figure 6), and the decoupling between $p\text{CO}_2$ and watershed land use (Figure 7) during the flooding season.

On the other hand, our results suggest that aquatic metabolism as an internal CO_2 source was more important than lateral CO_2 input in the Shanghai river network. This contrasts with a recent work by *Hotchkiss et al.* [2015], in which internal CO_2 production was found to contribute on average to 28% of CO_2 evasion from streams and rivers across the contiguous United States with the remainder being lateral inputs of terrestrial CO_2. The reason for this contrast is multifold. First, surface-subsurface water exchange is limited by hydromorphological constrains in this low-lying depositional system. Assuming a high groundwater CO_2 ($51,900$ µatm [*Johnson et al.*, 2008]), lateral groundwater inflow would need to be about 12% of surface water discharge to support 70% of the remaining CO_2 evasion (i.e., 2.8 g C m^{-2} d^{-1}) after accounting for the contribution of longitudinal input (i.e., 43%) along the Huangpu River main stem. Such high lateral influx is unrealistic on an annual basis in this lowland watershed where downwelling events frequently occur especially during the wet season [*Yin et al.*, 2013; *Wu et al.*, 2014]. Second, substantial OC and NH_4^+ inputs from nonpoint urban runoffs and WWTP effluents [*Yu et al.*, 2013] might stimulate metabolic CO_2 production. Using absorption and

fluorescence spectroscopy, *Guo et al.* [2014] measured concentration and quality of DOC near the Wusong Mouth. DOC concentration was much higher near the Wusong Mouth (~5 mg L^{-1}) than in the main stem of the Yangtze River (<2 mg L^{-1}) and protein-like components dominated the DOC composition (~73%), indicating that net heterotrophy was favored by anthropogenic input of bioavailable OC [*Wilson and Xenopoulos*, 2009; *Hosen et al.*, 2014;]. Moreover, NH_4^+, a riverine indicator of anthropogenic activities, was highly correlated with pCO_2 in the mainland river network (Table 2). Rapid nitrification driven by the high NH_4^+ concentrations (maximum site-averaged $NH_4^+ > 8$ mg N L^{-1}; Figure S7f) might significantly contribute to the consumption of DO and HCO_3^- alkalinity, producing ~2 mol of free CO_2 with every 1 mol of nitrified NH_4^+ (plus 2 mol of dissolved O_2) [*Dai et al.*, 2008]. Applying the nitrification rate constant measured for the polluted Pearl River (i.e., 0.089 day^{-1} [*Dai et al.*, 2008]) to the longitudinal transect of the Huangpu River (overall mean NH_4^+ concentration: 1.6 ± 0.9 mg N L^{-1}) indicated that nitrification-produced CO_2 could contribute to 47% of the modeled NEP (i.e., 2.4 g C m^{-2} d^{-1}). Therefore, although we did not explicitly separate nitrification from ecosystem respiration during the coupled DIC-CO_2-O_2 modeling, nitrification might have played a critical role in sustaining the CO_2 supersaturation and coupling pCO_2 with watershed land use during the dry season (Figure 7). Finally, anthropogenic alterations of the river morphology, including riverbank concretion, channel straightening, and riparian de-vegetation (Figure S2), might disrupt natural interactions between the rivers and their floodplains [*Sweeney et al.*, 2004], hampering lateral water and C exchanges in this human-dominated watershed.

It is important to note that the simple modeling approach adopted in this study only offers a coarse perspective on the relative importance of the identified major CO_2 sources, because it does not differentiate other possible pathways, and is based on annually averaged model inputs. Given the widespread CH_4 oversaturation (see below), locally reduced conditions are likely ubiquitous in the Shanghai river network. If anaerobic respiration was significant, that would reduce the estimated contribution of lateral input. Conversely, the lateral signal would be higher if nonrespiratory O_2 consumption (e.g., DOC photooxidation [*Cory et al.*, 2014], inputs of DO-depleted groundwater, or sewage [*Hall and Tank*, 2005]) constituted a significant portion of the total O_2 demand. Since DO was always and only measured during daytime, the estimated internal production might be biased low due to aquatic photosynthesis. Accordingly, our results not only provide preliminary insights into the biogeochemical and hydrological controls on the CO_2 supersaturation in this complex river network but also highlight the need for direct comparative quantification of different CO_2 sources and their temporal variations. Overall, our results stress the high sensitivity of river CO_2 dynamics to human activities in lowland coastal areas and provide initial evidence that these dynamics may be unique along the stream-river continuum.

4.2. Effects of Watershed Land Use on River CH_4 Dynamics

The Shanghai river network was supersaturated with respect to CH_4 during the entire study period (overall median: 241 μatm; Figures 4b and 4d). The measured pCH_4 in the Shanghai river network was generally higher than in temperate and subtropical streams but was generally lower than in boreal high-order rivers draining peatland watersheds (Table S1). The highest pCH_4 was measured in the urban fourth-order rivers (Figures 4b and 4d) having the most severe hypoxia and eutrophication (Figure S7). The landuse percentage and channel morphological properties were included in the MLR models (Table 2), despite the fact that these factors had a much lower data resolution than the water chemistry variables. In the PCA pCH_4 was always tightly coupled to the land use component (Figure 7). These observed spatial variations of pCH_4 suggest that the CH_4 supersaturation was due to development of localized anaerobic conditions in OC-enriched rivers.

The OC-enrich river environments and reducing conditions are not unique to the Shanghai river network, as similar results have been reported for other lowland high-order rivers draining watersheds of various land use [*Crawford et al.*, 2016]. Given the large DO deficiency throughout the river network (Figure S7a), it is likely that O_2 could be rapidly depleted in the river sediments, leading to anoxia in close proximity to the sediment surface. Although particulate organic carbon (POC) and DOC were not measured in this study, high concentrations of allochthonous POC and DOC can be expected in the urban rivers receiving nonpoint overland runoff [*Westerhoff and Anning*, 2000]. High POC and DOC loadings in conjunction with the stagnant flow velocity might promote lake-like sedimentary dynamics in central portion of the river channels [*Maeck et al.*, 2013] and, consequently, foster benthic methanogenesis. This OC burial-driven pathway of CH_4 production

might be particularly important for the small urban rivers where sediment area per water volume is relatively large [*Battin et al.*, 2008]. Additionally, the large DO deficiency and the enrichments of NH_4^+ and DOC in the water column might suppress CH_4 oxidation by methanotrophs [*Crombie and Murrell*, 2014; *Stanley et al.*, 2016], leading to net methanogenesis in the urban rivers.

Benthic methanogenesis as a localized CH_4 source in the urban rivers is also consistent with the decreased pCH_4 during the wet season when the river water CH_4 might be diluted by the increased upstream runoff (Figure 5b) [*Jones and Mulholland*, 1998]. This diluting effect is supported by the much lower pCH_4 observed in the headwater rivers (Figure 4b) and at all the network inlets (data not shown). The absence of a pulse-like pCH_4 increase during the flooding season indicates that longitudinal and lateral CH_4 inputs from floodplain soils or the upstream drainage system might only play a minor role in sustaining the CH_4 supersaturation and evasion in the Shanghai river network [*Jones and Mulholland*, 1998; *Anthony et al.*, 2012]. Moreover, given the low solubility of CH_4 and presumably enhanced k_{CH4} during high-flow events, the low contribution of external pathways might partially result from rapid CH_4 degassing during hydrological transport, creating spatially heterogeneous structure of pCH_4 along the river continuum [*Stanley et al.*, 2016].

It is worth noting that discharge of CH_4-rich WWTP effluents could directly contribute to pCH_4 supersaturation in the urban rivers and that this CH_4 source cannot be differentiated from sewage-fueled benthic methanogenesis in this analysis. This is because of the interrelated nature of these two sources such that they are expected to influence the spatiotemporal pattern of pCH_4 in a similar way. A recent study by *Alshboul et al.* [2016] found that CH_4 concentration in WWTP effluents ranged from 139 µatm to 4511 µatm and was 814 ± 1415 µatm on average for nine WWTPs in Southwest Germany (CH_4 concentrations were converted from µM to µatm by assuming 0‰ salinity and a temperature of 20°C). These concentrations are generally within the same range of the measured urban pCH_4 (overall median: 585 µatm) but lower than the high pCH_4 during the dry season (e.g., >10000 µatm; Figures 4b and 4d), indicating that the CH_4 supersaturation might be only partially sustained by direct effluent inputs on an annual basis. Further constraints on WWTP effluent load and its OC and CH_4 contents are needed to tease apart the relative importance of these two pathways in the urban rivers.

Therefore, we suggest that anthropogenic impacts must be considered when modeling CH_4 dynamics in human-impacted lowland coastal rivers. While CH_4 supply from adjoining floodplains may be remarkably reduced in highly engineered lowland urban rivers, concomitant increase in watershed impervious surface and WWTP effluent discharges can create spatially discrete hot spot for CH_4 production and evasion. These land use effects on river CH_4 dynamics need to be carefully considered as action is taken to recover ecological and biogeochemical benefits from urban river systems [*Anthony et al.*, 2012].

4.3. Importance of Riverine CO_2 and CH_4 Evasions in Coastal C Budget

The estimated fCO_2 (overall mean: 7.81 ± 3.83 g C m^{-2} d^{-1}) and fCH_4 (overall median: 11.6 mg C m^{-2} d^{-1}) in the Shanghai river network are well within the range reported for high-order rivers worldwide but generally lower than those found in headwater streams having high connectivity with surrounding landscapes (Table S1). More specifically, the estimated fCO_2 was consistent with previous measurements in large Chinese rivers draining highly urbanized landscapes (e.g., 10.5 ± 6.6 g C m^{-2} d^{-1}, Chongqing urban river network, China [*Wang et al.*, 2017]) and average CO_2 emission from global streams and rivers, i.e., 7.9 mg C m^{-2} d^{-1} (calculated by dividing global total emission, 1800 Tg C yr^{-1}, by global stream and river surface area, 624,000 km^2) [*Raymond et al.*, 2013]. On the other hand, our k_{600} used for the flux estimation is at the lower end of the range reported for streams and rivers and apparently less variable than those directly measured in large rivers (Figure 3 and Table S1), indicating that pCO_2 exerted a more significant control on the estimated fCO_2. Additionally, our method may underestimate fCO_2 because samples were always taken during daytime when pCO_2 might be reduced by photosynthetic CO_2 uptake [*Crawford et al.*, 2014]. Because ebullitive CH_4 evasion was not included, our estimates on fCH_4, representing only the diffusive component, can also be considered highly conservative. Since large coastal rivers may occupy a unique position in the river continuum where turbulence controlling k_{600} is modulated by a dynamic combination of upstream runoff, tidal currents, and wind [*Alin et al.*, 2011], direct k_{600} measurements are needed to further refine the flux estimation.

Zhai et al. [2007] measured total DIC concentrations near the Wusong Mouth and estimated that annual DIC export from the Huangpu River was 0.28 Tg C yr^{-1}. Therefore, despite the potential underestimations on fCO$_2$, the ratio of CO$_2$ evasion to DIC export for the mainland river network was approximately 4.1:1, higher than those for the Mississippi River basin (0.9:1 [*Dubois et al.*, 2010]) and the Yukon River basin (1:1 [*Striegl et al.*, 2012]). If the upstream watershed that contributed to the DIC export was included in the evasion esti-mate, the C evasion/export ratio of the Shanghai river network could be potentially comparable to those for the Yellow River basin (4.7:1 [*Ran et al.*, 2015]) and the Amazon basin (6.6:1 [*Richey et al.*, 2002]). The revealed high evasion/export ratio is partially due to the large river surface area in this lowland region (~9%) but also highlights the potential of lowland coastal rivers as open reactors mineralizing terrestrial and anthropogenic OC and wide conduits for CO$_2$ evasion near the end of the stream-river continuum.

From the perspective of atmospheric radiative forcing, CH$_4$ evasion was much less important than CO$_2$ eva-sion in the Shanghai river network, although it was higher than the total CH$_4$ emission from the estuarine wetlands of the Yangtze River (Table 3). CO$_2$ evasion from the river network was comparable to CH$_4$ emission from rice fields in Shanghai, an anthropogenic C emission source broadly concerned for the lower Yangtze River basin [*Li et al.*, 2005]. Based on NEP data measured at three cropland and forest sites in the upper Taihu Lake basin, *Xu et al.* [2017] estimated that terrestrial NEP was 6.7 Tg CO$_2$-eq yr^{-1} for the Shanghai City and ranged between 44.7 Tg CO$_2$-eq yr^{-1} and 55.8 Tg CO$_2$-eq yr^{-1} for the entire Tailu Lake basin. To place the river CO$_2$ evasion in the context of terrestrial NEP, we can make an upper boundary estimate of river emissions relative to terrestrial NEP for the Shanghai City by accounting for the contribution of external input through longitudinal pathways, that is, 43% of the total emission (Figure 8), and assuming that most local CO$_2$ inputs to the rivers via internal production and lateral input are of terrestrial origin. Therefore, our estimate of river CO$_2$ emissions is ~40% of terrestrial NEP of the Shanghai City. While the magnitude of this offset is among the highest in the literature [*Butman et al.*, 2016], the inability to assess the fraction of the related C fluxes derived from anthropogenic sources (e.g., WWTP effluent discharges and nitrification) biases this esti-mate high. On the other hand, given that the Shanghai river network covers only about 20% of the surface water area of the Taihu Lake basin (i.e., 2800 km^2, excluding the Taihu Lake), the total CO$_2$ emission from the Shanghai river network indicates that a minimum of 10% of the estimated NEP may be offset at the basin scale (Table 3), reinforcing the need to accurately account for aquatic C fluxes in watershed C budgets [*Raymond et al.*, 2013; *Butman et al.*, 2016]. Furthermore, there is growing evidence that nutrient exports via the Yangtze River fuel GPP of the river-dominated East China Sea, creating a net C sink of -47.5 Tg CO$_2$-eq yr^{-1} [*Tseng et al.*, 2014]. In this context, CO$_2$ evasion from the Shanghai river network offsets about 10% of this C sink, although the Shanghai river network is only less than 0.1% of the river-dominated East China Sea by area (Table 3). Given that 75% of world's population is predicted to live in coastal areas by 2025 [*Bianchi and Allison*, 2009], attribution of CO$_2$ evasion from coastal river networks to anthropogenic driving forces represents an important research avenue for understanding the role that coastal ecosystems can play in regional and global C cycles.

5. Conclusions

With about 60% of the world population living along global coastal boundaries, a mechanistic understanding of the processes regulating C dynamics in human-dominated lowland coastal rivers is essential for sound prediction of the present and future role of coastal ecosystems in global C cycling. In this study, we reported results from a long-term, large-scale study of pCO$_2$ and pCH$_4$ in the Shanghai river network, one of the world's largest lowland coastal watersheds subject to profound human perturbations. CO$_2$ and CH$_4$ evasions rates were estimated based on a wind-based k_{600} parameterization and then used to assess the role of river C emissions in regional C budget. During the study period, the overall mean pCO$_2$ and median pCH$_4$ from 87 surveyed rivers were 5846 ± 2773 µatm and 241 µatm, respectively. While the CH$_4$ supersaturation was closely associated with urban land use, the spatiotemporal variability of pCO$_2$ was modulated by both biogeochemical and hydrological controls. Using a coupled DIC-CO$_2$-O$_2$ model, we estimated that major CO$_2$ sources sustaining the CO$_2$ supersaturation and evasion in the Shanghai river network were (1) net heterotrophy and nitrification promoted by anthropogenic inputs of OC and NH$_4^+$ and (2) longitudinal input of CO$_2$ originating from aquatic and terrestrial respiration in the upstream watersheds. While the former challenges the river continuum concept that downstream ecosystems are geophysically constrained to be

energy-deficient, the latter represents a legacy of widespread perturbations on the aquatic system in this human-dominated coastal area. Due to the limited surface-subsurface water exchange as well as the substantial CO_2 input from internal production, lateral CO_2 input via groundwater was only a minor source contributing to the CO_2 supersaturation and evasion, suggesting a spatially heterogeneous nature of land-water C interaction along a theoretical stream-river continuum. The estimated annual CO_2 emission indicates that river CO_2 evasion offsets up to 40% of terrestrial NEP of the Shanghai City and 10% of net C uptake in the river-dominated East China Sea. Our findings reinforce the notion that aquatic C fluxes must be included in larger-scale C budgets to constrain terrestrial C cycling and fate and highlight a pressing need to elucidate anthropogenic controls on C dynamics in land-water budgets.

References

Abril, G., et al. (2014), Amazon River carbon dioxide outgassing fuelled by wetlands, *Nature*, *505*(7483), 395–398, doi:10.1038/nature12797.

Alin, S. R., M. F. F. L Rasera, C. I. Salimon, J. E. Richey, G. W. Holtgrieve, A. V. Krusche, and A. Snidvongs (2011), Physical controls on carbon dioxide transfer velocity and flux in low-gradient river systems and implications for regional carbon budgets, *J. Geophys. Res.*, *116*, G01009, doi:10.1029/2010JG001398.

Alshboul, Z., J. Encinas-Fernández, H. Hofmann, and A. Lorke (2016), Export of dissolved methane and carbon dioxide with effluents from municipal wastewater treatment plants, *Environ. Sci. Technol.*, *50*(11), 5555–5563, doi:10.1021/acs.est.5b04923.

Anthony, S. E., F. G. Prahl, and T. D. Peterson (2012), Methane dynamics in the Willamette River, Oregon, *Limnol. Oceanogr.*, *57*(5), 1517–1530, doi:10.4319/lo.2012.57.5.1517.

Aufdenkampe, A. K., E. Mayorga, P. A. Raymond, J. M. Melack, S. C. Doney, S. R. Alin, R. E. Aalto, and K. Yoo (2011), Riverine coupling of biogeochemical cycles between land, oceans, and atmosphere, *Front. Ecol. Environ.*, *9*(1), 53–60, doi:10.1890/100014.

Bastviken, D., L. J. Tranvik, J. A. Downing, P. M. Crill, and A. Enrich-Prast (2011) Freshwater methane emissions offset the continental carbon sink, *Science*, *331*(6013), 50–50, doi:10.1126/science.1196808.

Battin, T. J., L. A. Kaplan, S. Findlay, C. S. Hopkinson, E. Marti, A. I. Packman, J. D. Newbold, and F. Sabater (2008), Biophysical controls on organic carbon fluxes in fluvial networks, *Nat. Geosci.*, *1*(2), 95–100, doi:10.1038/ngeo101.

Battin, T. J., S. Luyssaert, L. A. Kaplan, A. K. Aufdenkampe, A. Richter, and L. J. Tranvik (2009), The boundless carbon cycle, *Nat. Geosci.*, *2*(9), 598–600, doi:10.1038/ngeo618.

Beaulieu, J. J., W. D. Shuster, and J. A. Rebholz (2012), Controls on gas transfer velocities in a large river, *J. Geophys. Res.*, *117*, G02007, doi:10.1029/2011JG001794.

Bianchi, T. S., and M. A. Allison (2009), Large-river delta-front estuaries as natural "recorders" of global environmental change, *Proc. Natl. Acad. Sci. U.S.A.*, *106*(20), 8085–8092, doi:10.1073/pnas.0812878106.

Billett, M. F., and T. R. Moore (2008), Supersaturation and evasion of CO_2 and CH_4 in surface waters at Mer Bleue peatland, Canada, *Hydrol. Process.*, *22*(12), 2044–2054, doi:10.1002/hyp.6805.

Borges, A. V., J. Vanderborght, L. S. Schiettecatte, F. Gazeau, S. Ferrón-Smith, B. Delille, and M. Frankignoulle (2004), Variability of the gas transfer velocity of CO_2 in a macrotidal estuary (the Scheldt), *Estuaries*, *27*(4), 593–603.

Butman, D., and P. A. Raymond (2011), Significant efflux of carbon dioxide from streams and rivers in the United States, *Nat. Geosci.*, *4*(12), 839–842, doi:10.1038/ngeo1294.

Butman, D. E., H. F. Wilson, R. T. Barnes, M. A. Xenopoulos, and P. A. Raymond (2015), Increased mobilization of aged carbon to rivers by human disturbance, *Nat. Geosci.*, *8*(2), 112–116, doi:10.1038/ngeo2322.

Butman, D., S. Stackpoole, E. Stets, C. P. McDonald, D. W. Clow, and R. G. Striegl (2016), Aquatic carbon cycling in the conterminous United States and implications for terrestrial carbon accounting, *Proc. Natl. Acad. Sci. U.S.A.*, *113*(1), 58–63, doi:10.1073/pnas.1512651112.

Campeau, A., J. F. Lapierre, D. Vachon, and P. A. Giorgio (2014), Regional contribution of CO_2 and CH_4 fluxes from the fluvial network in a lowland boreal landscape of Québec, *Global Biogeochem. Cycles*, *28*, 57–69, doi:10.1002/2013GB004685.

Cole, J. J., et al. (2007), Plumbing the global carbon cycle: Integrating inland waters into the terrestrial carbon budget, *Ecosystems*, *10*(1), 172–185, doi:10.1007/s10021-006-9013-8.

Chetelat, B., C. Q. Liu, Z. Zhao, Q. Wang, S. Li, J. Li, and B. Wang (2008), Geochemistry of the dissolved load of the Changjiang Basin rivers: Anthropogenic impacts and chemical weathering, *Geochim. Cosmochim. Acta*, *72*(17), 4254–4277, doi:10.1016/j.gca.2008.06.013.

Cory, R. M., C. P. Ward, B. C. Crump, and G. W. Kling (2014), Sunlight controls water column processing of carbon in arctic fresh waters, *Science*, *345*(6199), 925–928, doi:10.1126/science.1253119.

Crawford, J. T., R. G. Striegl, K. P. Wickland, M. M. Dornblaser, and E. H. Stanley (2013), Emissions of carbon dioxide and methane from a headwater stream network of interior Alaska, *J. Geophys. Res. Biogeosci.*, *118*, 482–494, doi:10.1002/jgrg.20034.

Crawford, J. T., N. R. Lottig, E. H. Stanley, J. F. Walker, P. C. Hanson, J. C. Finlay, and R. G. Striegl (2014), CO_2 and CH_4 emissions from streams in a lake-rich landscape: Patterns, controls, and regional significance, *Global Biogeochem. Cycles*, *28*, 197–210, doi:10.1002/2013GB004661.

Crawford, J. T., L. C. Loken, E. H. Stanley, E. G. Stets, M. M. Dornblaser, and R. G. Striegl (2016), Basin scale controls on CO_2 and CH_4 emissions from the Upper Mississippi River, *Geophys. Res. Lett.*, *43*, 1973–1979, doi:10.1002/2015GL067599.

Crombie, A. T., and J. C. Murrell (2014), Trace-gas metabolic versatility of the facultative methanotroph Methylocella silvestris, *Nature*, *510*, 148–151, doi:10.1038/nature13192.

Dai, M., L. Wang, X. Guo, W. Zhai, Q. Li, B. He, and S. J. Kao (2008), Nitrification and inorganic nitrogen distribution in a large perturbed river/estuarine system: The Pearl River Estuary, China, *Biogeosciences*, *5*, 1227–1244, doi:10.5194/bg-5-1227-2008.

Dinsmore, K. J., M. F. Billett, U. M. Skiba, R. M. Rees, J. Drewer, and C. Helfter (2010), Role of the aquatic pathway in the carbon and greenhouse gas budgets of a peatland catchment, *Global Change Biol.*, *16*(10), 2750–2762, doi:10.1111/j.1365-2486.2009.02119.x.

Downing, J. A., J. J. Cole, C. A. Duarte, J. J. Middelburg, J. M. Melack, Y. T. Prairie, P. Kortelainen, R. G. Striegl, W. H. McDowell, and L. J. Tranvik (2012), Global abundance and size distribution of streams and rivers, *Inland Waters*, *2*(4), 229–236, doi:10.5268/iw-2.4.502.

Driscoll, C. T., R. D. Fuller, and W. D. Schecher (1989), The role of organic acids in the acidification of surface waters in the eastern US, *Water Air Soil Pollut.*, *43*(1), 21–40, doi:10.1007/BF00175580.

Dubois, K. D., D. Lee, and J. Veizer (2010), Isotopic constraints on alkalinity, dissolved organic carbon, and atmospheric carbon dioxide fluxes in the Mississippi River, *J. Geophys. Res.*, *115*, G02018, doi:10.1029/2009JG001102

IPCC (2007), Changes in atmospheric constituents and in radiative forcing, in *Climate Change 2007: The Physical Science Basis. Contribution of Working Group I to the Fourth Assessment Report of the Intergovernmental Panel on Climate Change*, edited by S. Solomon, et al., pp. 129–234, Cambridge Univ. Press, Cambridge.

Guo, W., L. Yang, W. Zhai, W. Chen, C. L. Osburn, X. Huang, and Y. Li (2014), Runoff-mediated seasonal oscillation in the dynamics of dissolved organic matter in different branches of a large bifurcated estuary—The Changjiang Estuary, *J. Geophys. Res. Biogeosci.*, *119*, 776–793, doi:10.1002/2013jg002540.

Guérin, F., G. Abril, D. Serça, C. Delon, S. Richard, R. Delmas, A. Tremblay, and L. Varfalvy (2007), Gas transfer velocities of CO_2 and CH_4 in a tropical reservoir and its river downstream, *J. Mar. Syst.*, *66*(1), 161–172, doi:10.1016/j.jmarsys.2006.03.019.

Gómez-Gener, L., D. Schiller, R. Marcé, M. Arroita, J. P. Casas-Ruiz, P. A. Staehr, V. Acuña, S. Sabater, and B. Obrador (2016), Low contribution of internal metabolism to carbon dioxide emissions along lotic and lentic environments of a Mediterranean fluvial network, *J. Geophys. Res. Biogeosci.*, *121*, 3030–3044, doi:10.1002/2016JG003549.

Hall, R. O., and J. L. Tank (2005), Correcting whole-stream estimates of metabolism for groundwater input, *Limnol. Oceanogr. Methods*, *3*(4), 222–229, doi:10.4319/lom.2005.3.222.

Humborg, C., C. MÖRTH, M. Sundbom, H. Borg, T. Blenckner, R. Giesler, and V. Ittekkot (2010), CO_2 supersaturation along the aquatic conduit in Swedish watersheds as constrained by terrestrial respiration, aquatic respiration and weathering, *Global Change Biol.*, *16*, 1966–1978, doi:10.1111/j.1365-2486.2009.02092.x.

Hoellein, T. J., D. A. Bruesewitz, and D. C. Richardson (2013), Revisiting Odum (1956), A synthesis of aquatic ecosystem metabolism, *Limnol. Oceanogr.*, *58*(6), 2089–2100, doi:10.4319/lo.2013.58.6.2089.

Hope, D., S. M. Palmer, M. F. Billett, and J. J. C. Dawson (2001), Carbon dioxide and methane evasion from a temperate peatland stream, *Limnol. Oceanogr.*, *46*(4), 847–857, doi:10.4319/lo.2001.46.4.0847.

Hosen, J. D., O. T. McDonough, C. M. Febria, and M. A. Palmer (2014), Dissolved organic matter quality and bioavailability changes across an urbanization gradient in headwater screams, *Environ. Sci. Technol.*, *48*(4), 7817–7824, doi:10.1021/es501422z.

Hotchkiss, E. R., R. O. Hall Jr., R. A. Sponseller, D. Butman, J. Klaminder, H. Laudon, M. Rosvall, and J. Karlsson (2015), Sources of and processes controlling CO_2 emissions change with the size of streams and rivers, *Nat. Geosci.*, *8*(9), 696–699, doi:10.1038/ngeo2507.

Jähne, B., K. O. Münnich, R. Bösinger, A. Dutzi, W. Huber, and P. Libner (1987), On the parameters influencing air-water gas exchange, *J. Geophys. Res.*, *92*(C2), 1937–1949, doi:10.1029/JC092ic02p01937.

Johnson, M. S., J. L. Lehmann, S. J. Riha, A. V. Krusche, J. F. Richey, J. P. H. B. Ometto, and E. G. Couto (2008), CO_2 efflux from Amazonian headwater streams represents a significant fate for deep soil respiration, *Geophys. Res. Lett.*, *35*, L17401, doi:10.1029/2008GL034619.

Jones, J. B., and P. J. Mulholland (1998), Methane input and evasion in a hardwood forest stream: Effects of subsurface flow from shallow and deep pathway, *Limnol. Oceanogr.*, *43*(6), 1243–1250, doi:10.4319/lo.1998.43.6.1243.

Kaushal, S. S., K. Delaney-Newcomb, S. E. G. Findlay, T. A. Newcomer, S. Duan, M. J. Pennino, G. M. Sivirichi, A. M. Sides-Raley, M. R. Walbridge, and K. T. Belt (2014), Longitudinal patterns in carbon and nitrogen fluxes and stream metabolism along an urban watershed continuum, *Biogeochemistry*, *121*(1), 23–44, doi:10.1007/s10533-014-9979-9.

Kokic, J., M. B. Wallin, H. E. Chmiel, B. A. Denfeld, and S. Sobek (2015), Carbon dioxide evasion from headwater systems strongly contributes to the total export of carbon from a small boreal lake catchment, *J. Geophys. Res. Biogeosci.*, *120*, 13–28, doi:10.1002/2014JG002706.

Li, C., S. Frolking, X. Xiao, B. Moore, S. Boles, J. Qiu, Y. Huang, W. Salas, and R. Sass (2005), Modeling impacts of farming management alternatives on CO_2, CH_4, and N_2O emissions: A case study for water management of rice agriculture of China, *Global Biogeochem. Cycles*, *19*, GB3010, doi:10.1029/2004GB002341.

Lundin, E. J., R. Giesler, A. Persson, M. S. Thompson, and J. Karlsson (2013), Integrating carbon emissions from lakes and streams in a subarctic catchment, *J. Geophys. Res. Biogeosci.*, *118*, 1200–1207, doi:10.1002/jgrg.20092.

Maeck, A., T. DelSontro, D. F. McGinnis, H. Fischer, S. Flury, M. Schmidt, P. Fietzek, and A. Lorke (2013), Sediment trapping by dams creates methane emission hot spots, *Environ. Sci. Technol.*, *47*(15), 8130–8137, doi:10.1021/es4003907.

Mayorga, E., A. K. Aufdenkampe, C. A. Masiello, A. V. Krusche, J. I. Hedges, P. D. Quay, J. E. Richey, and T. A. Brown (2005), Young organic matter as a source of carbon dioxide outgassing from Amazonian rivers, *Nature*, *436*(7050), 538–541, doi:10.1038/nature03880.

Mileyko, Y., H. Edelsbrunner, C. A. Price, and J. S. Weitz (2012), Hierarchical ordering of reticular networks, *PLoS One*, *7*(6), e36715, doi:10.1371/journal.pone.0036715.

Millero, F. J. (2007), The marine inorganic carbon cycle, *Chem. Rev.*, *107*(2), 308–341, doi:10.1021/cr0503557.

Noriega, C., and M. Araujo (2014), Carbon dioxide emissions from estuaries of northern and northeastern Brazil, *Sci. Rep.*, *4*, 6164, doi:10.1038/srep06164.

Öquist, M. G., M. Wallin, J. Seibert, K. Bishop, and H. Laudon (2009), Dissolved inorganic carbon export across the soil/stream interface and its fate in a boreal headwater stream, *Environ. Sci. Technol.*, *43*(19), 7364–7369, doi:10.1021/es900416h.

Panneer Selvam, B., S. Natchimuthu, L. Arunachalam, and D. Bastviken (2014), Methane and carbon dioxide emissions from inland waters in India—Implications for large scale greenhouse gas balances, *Global Change Biol.*, *20*(11), 3397–3407, doi:10.1111/gcb.12575.

Pérez, C. A., M. S. DeGrandpre, N. A. Lagos, G. S. Saldías, E. K. Cascales, and C. A. Vargas (2015), Influence of climate and land use in carbon biogeochemistry in lower reaches of rivers in central southern Chile: Implications for the carbonate system in river-influenced rocky shore environments, *J. Geophys. Res. Biogeosci.*, *120*, 673–692, doi:10.1002/2014JG002699.

Ran, L., X. X. Lu, H. Yang, L. Li, R. Yu, H. Sun, and J. Han (2015), CO_2 outgassing from the Yellow River network and its implications for riverine carbon cycle, *J. Geophys. Res. Biogeosci.*, *120*, 1334–1347, doi:10.1002/2015JG002982.

Ran, L., X. X. Lu, and S. Liu (2017), Dynamics of riverine CO_2 in the Yangtze River fluvial network and their implications for carbon evasion, *Biogeosciences*, *14*(8), 2183–2198, doi:10.5194/bg-14-2183-2017.

Rasera, M. F. F. L., A. V. Krusche, J. E. Richey, M. V. R. Ballester, and R. L. Victória (2013), Spatial and temporal variability of pCO_2 and CO_2 efflux in seven Amazonian rivers, *Biogeochemistry*, *116*(1–3), 241–259.

Rasilo, T., Y. T. Prairie, and P. A. Giorgio (2015), Large-scale patterns in summer diffusive CH_4 fluxes across boreal lakes, and contribution to diffusive C emissions, *Global Change Biol.*, *21*(3), 1124–1139, doi:10.1007/s10533-013-9854-0.

Raymond, P. A., and J. J. Cole (2001), Gas exchange in rivers and estuaries: Choosing a gas transfer velocity, *Estuaries Coasts*, *24*(2), 312–317, doi:10.2307/1352954.

Raymond, P. A., C. J. Zappa, D. Butman, T. L. Bott, J. Potter, P. Mulholland, A. E. Laursen, W. H. McDowell, and D. Newbold (2012), Scaling the gas transfer velocity and hydraulic geometry in streams and small rivers, *Limnol. Oceanogr.*, *2*(1), 41–53, doi:10.1215/21573689-1597669.

Raymond, P. A., et al. (2013), Global carbon dioxide emissions from inland waters, *Nature*, *503*, 355–359, doi:10.1038/nature12760.

Regnier, P., et al. (2013), Anthropogenic perturbation of the carbon fluxes from land to ocean, *Nat. Geosci.*, *6*, 597–607, doi:10.1038/ngeo1830.

Richey, J. E., J. M. Melack, A. K. Aufdenkampe, V. M. Ballester, and L. L. Hess (2002), Outgassing from Amazonian rivers and wetlands as a large tropical source of atmospheric CO_2, *Nature*, *416*, 617–620, doi:10.1038/416617a.

Sawakuchi, H. O., D. Bastviken, A. O. Sawakuchi, A. V. Krusche, M. V. R. Ballester, and J. E. Richey (2014), Methane emissions from Amazonian rivers and their contribution to the global methane budget, *Global Change Biol.*, *20*(9), 2829–2840, doi:10.1111/gcb.12646.

Smith, R. M., and S. S. Kaushal (2015), Carbon cycle of an urban watershed: Exports, sources, and metabolism, *Biogeochemistry*, *126*(1–2), 173–195, doi:10.1007/s10533-015-0151-y.

Stanley, E. H., N. J. Casson, S. T. Christel, J. T. Crawford, L. C. Loken, and S. K. Oliver (2016), The ecology of methane in streams and rivers: Patterns, controls, and global significance, *Ecol. Monogr.*, *86*(12), 146–171, doi:10.1890/15-1027.

Stets, E. G., D. Butman, C. P. McDonald, S. M. Stackpoole, M. D. DeGrandpre, and R. G. Striegl (2017), Carbonate buffering and metabolic controls on carbon dioxide in rivers, *Global Biogeochem. Cycles*, *31*, 663–677, doi:10.1002/2016GB005578.

Striegl, R. G., M. M. Dornblaser, C. P. McDonald, J. R. Rover, and E. G. Stets (2012), Carbon dioxide and methane emissions from the Yukon River system, *Global Biogeochem. Cycles*, *26*, GB0E05, doi:10.1029/2012GB004306.

Sweeney, B. W., T. L. Bott, J. K. Jackson, L. A. Kaplan, J. D. Newbold, L. J. Standley, W. C. Hession, and R. J. Horwitz (2004), Riparian deforestation, stream narrowing, and loss of stream ecosystem services, *Proc. Natl. Acad. Sci. U.S.A.*, *101*(39), 14,132–14,137, doi:10.1073/pnas.0405895101.

Tao, Y., Z. Yuan, W. Fengchang, and M. Wei (2013), Six-decade change in water chemistry of large freshwater Lake Taihu, China, *Environ. Sci. Technol.*, *47*(16), 9093–9101, doi:10.1021/es401517h.

Tranvik, L. J., et al. (2009), Lakes and reservoirs as regulators of carbon cycling and climate, *Limnol. Oceanogr.*, *54*(6), 2298–2314, doi:10.4319/lo.2009.54.6_part_2.2298.

Tseng, C. M., P. Y. Shen, and K. K. Liu (2014), Synthesis of observed air–sea CO_2 exchange fluxes in the river-dominated East China Sea and improved estimates of annual and seasonal net mean fluxes, *Biogeosciences*, *11*(14), 3855–3870, doi:10.5194/bg-11-3855-2014.

Wang, Z. A., D. J. Bienvenu, P. J. Mann, K. A. Hoering, J. A. Poulsen, R. G. M. Spencer, and R. M. Holmes (2013), Inorganic carbon speciation and fluxes in the Congo River, *Geophys. Res. Lett.*, *40*, 511–516, doi:10.1002/grl.50160.

Wallin, M., I. Buffam, M. Öquist, H. Laudon, and K. Bishop (2010), Temporal and spatial variability of dissolved inorganic carbon in a boreal stream network: Concentrations and downstream fluxes, *J. Geophys. Res.*, *115*, G02014, doi:10.1029/2009JG001100.

Wang, D., Z. Chen, and S. Xu (2009), Methane emission from Yangtze estuarine wetland, China, *J. Geophys. Res.*, *114*, G02011, doi:10.1029/2008JG000857.

Wang, X., Y. He, X. Yuan, H. Chen, C. Peng, Q. Zhu, J. Yue, H. Ren, W. Deng, and H. Liu (2017), pCO_2 and CO_2 fluxes of the metropolitan river network in relation to the urbanization of Chongqing, China, *J. Geophys. Res. Biogeosci.*, *122*, 470–486, doi:10.1002/2016JG003494.

Weiss, R. F. (1970), The solubility of nitrogen, oxygen and argon in water and seawater, *Deep Sea Res. Oceanogr. Abstr.*, *17*(4), 721–735, doi:10.1016/0011-7471(70)90037-9.

Weiss, R. F. (1974), Carbon dioxide in water and seawater: The solubility of a non-ideal gas, *Mar. Chem.*, *2*(3), 203–215, doi:10.1016/0304-4203(74)90015-2.

Westerhoff, P., and D. Anning (2000), Concentrations and characteristics of organic carbon in surface water in Arizona: Influence of urbanization, *J. Hydrol.*, *236*(3–4), 202–222, doi:10.1016/s0022-1694(00)00292-4.

Wiesenburg, D. A., and N. L. Guinasso Jr (1979), Equilibrium solubilities of methane, carbon monoxide, and hydrogen in water and sea water, *J. Chem. Eng. Data*, *24*(4), 356–360, doi:10.1021/je60083a006.

Wilson, H. F., and M. A. Xenopoulos (2009), Effects of agricultural land use on the composition of fluvial dissolved organic matter, *Nat. Geosci.*, *2*(1), 37–41, doi:10.1038/ngeo391.

Winterdahl, M., M. B. Wallin, R. H. Karlsen, H. Laudon, M. Öquist, and S. W. Lyon (2016), Decoupling of carbon dioxide and dissolved organic carbon in boreal headwater streams, *J. Geophys. Res. Biogeosci.*, *121*, 2630–2651, doi:10.1002/2016JG003420.

Wu, C., G. Ye, L. Zhang, D. Bishop, and J. Wang (2014), Depositional environment and geotechnical properties of Shanghai clay: A comparison with Ariake and Bangkok clays, *Bull. Eng. Geol. Environ.*, *74*(3), 1–16, doi:10.1007/s10064-014-0670-0.

Xu, X., G. Yang, Y. Tan, X. Tang, H. Jiang, X. Sun, Q. Zhuang, and H. Li (2017), Impacts of land use changes on net ecosystem production in the Taihu Lake Basin of China from 1985 to 2010, *J. Geophys. Res. Biogeosci.*, *122*, 690–707, doi:10.1002/2016JG003444.

Xu, S, J. Shu, and Z. Wang (2004), *Atlas of Shanghai Urban Physical Geography*, pp. 56–58, China Map Press, Shanghai.

Yin, J., D. Yu, Z. Yin, J. Wang, and S. Xu (2013), Multiple scenario analyses of Huangpu River flooding using a 1D/2D coupled flood inundation model, *Nat. Hazards*, *66*(2), 577–589, doi:10.1007/s11069-012-0501-1.

Yu, Z., H. Deng, D. Wang, M. Ye, Y. Tan, Y. Li, Z. Chen, and S. Xu (2013), Nitrous oxide emissions in the shanghai river network: Implications for the effects of urban sewage and IPCC methodology, *Global Change Biol.*, *19*(10), 2999–3010, doi:10.1111/gcb.12290.

Yuan, W., and K. Yang (2011), A method of catchments health assessment under value-pressure model and its application in urbanized river network area: A case study in Shanghai, China, *Chin. Geogr. Sci.*, *21*, 102–109, doi:10.1007/s11769-010-0435-z.

Zhai, W., M. Dai, and X. Guo (2007), Carbonate system and CO_2 degassing fluxes in the inner estuary of Changjiang (Yangtze) River, China, *Mar. Chem.*, *107*(3), 342–356, doi:10.1016/j.marchem.2007.02.011.

Zhang, G., J. Zhang, S. Liu, J. Ren, J. Xu, and F. Zhang (2008), Methane in the Changjiang (Yangtze River) estuary and its adjacent marine area: Riverine input, sediment release and atmospheric fluxes, *Biogeochemistry*, *91*(1), 71–84, doi:10.1007/s10533-008-9259-7.

Zhao, J., L. Lin, K. Yang, Q. Liu, and G. Qian (2015), Influences of land use on water quality in a reticular river network area: A case study in Shanghai, China, *Landscape Urban Plan.*, *137*, 20–29, doi:10.1016/j.landurbplan.2014.12.010.